

# One-Minute Resolution GOES-R Observations of Lamb and Gravity Waves Triggered by the Hunga Tonga-Hunga Ha'apai Eruptions on 15 January 2022

Akos Horvath<sup>1</sup>, Sharon L. Vadas<sup>2</sup>, Claudia Christine Stephan<sup>3</sup>, and Stefan Alexander Buehler<sup>4</sup>

<sup>1</sup>University of Hamburg

<sup>2</sup>NorthWest Research Associates, Inc.

<sup>3</sup>Max Planck Institute for Meteorology

<sup>4</sup>Universität Hamburg

January 18, 2024

1           **One-Minute Resolution GOES-R Observations of Lamb and Gravity Waves**  
2           **Triggered by the Hunga Tonga-Hunga Ha'apai Eruptions on 15 January 2022**

3  
4   **Ákos Horváth<sup>1</sup>, Sharon L. Vadas<sup>2</sup>, Claudia C. Stephan<sup>3</sup>, and Stefan A. Buehler<sup>1</sup>**

5   <sup>1</sup>Meteorological Institute, Universität Hamburg, Hamburg, Germany, <sup>2</sup>Northwest Research  
6   Associates, Boulder, Colorado, USA, <sup>3</sup>Leibniz Institute of Atmospheric Physics, University of  
7   Rostock, Kühlungsborn, Germany

8  
9   Corresponding author: Ákos Horváth (hfakos@gmail.com)

10  
11  
12   **Key Points:**

- 13       • Propagation of surface pressure anomalies explains the Lamb waveform derivative  
14       patterns seen in brightness temperature image differences  
15  
16       • 1-min mesoscale imagery depicts the short-period variations within the long-period wave  
17       packet envelope captured in full disk imagery  
18  
19       • The Lamb wave train appears dispersive, main pulse is followed by waves with  
20       decreasing wavelength of ~40–80 km and period of ~2.1–4.2 min

## 23 **Abstract**

24 We use high temporal-resolution mesoscale imagery from the Geostationary Operational  
25 Environmental Satellite-R (GOES-R) series to track the Lamb and gravity waves generated by  
26 the 15 January 2022 Hunga Tonga-Hunga Ha’apai eruption. The 1-min cadence of these limited  
27 area ( $\sim 1,000 \times 1,000 \text{ km}^2$ ) brightness temperatures ensures an order of magnitude better temporal  
28 sampling than full-disk imagery available at 10-min or 15-min cadence. The wave patterns are  
29 visualized in brightness temperature image differences, which represent the time derivative of  
30 the full waveform with the level of temporal aliasing being determined by the imaging cadence.  
31 Consequently, the mesoscale data highlight short-period variations, while the full-disk data  
32 capture the long-period wave packet envelope. The full temperature anomaly waveform,  
33 however, can be reconstructed reasonably well from the mesoscale waveform derivatives. The  
34 reconstructed temperature anomaly waveform essentially traces the surface pressure anomaly  
35 waveform. The 1-min imagery reveals waves with  $\sim 40\text{--}80 \text{ km}$  wavelengths, which trail the  
36 primary Lamb pulse emitted at  $\sim 04:29 \text{ UTC}$ . Their estimated propagation speed is  $\sim 315 \pm 15 \text{ m s}^{-1}$ ,  
37 resulting in typical periods of 2.1–4.2 min. Weaker Lamb waves were also generated by the  
38 last major eruption at  $\sim 08:40\text{--}08:45 \text{ UTC}$ , which were, however, only identified in the near field  
39 but not in the far field. We also noted wind effects such as mean flow advection in the  
40 propagation of concentric gravity wave rings and observed gravity waves traveling near their  
41 theoretical maximum speed.

## 42 **Plain Language Summary**

43 The record-setting eruption of the Hunga Tonga-Hunga Ha’apai volcano on 15 January 2022 was  
44 observed by geostationary satellites, which take an image of the full Earth disk every 10–15 min.  
45 Several smaller areas ( $\sim 1,000 \text{ km}$  on a side) are, however, imaged every 1 min. The eruption  
46 generated various waves in the atmosphere, including acoustic waves traveling at the speed of  
47 sound and slower gravity waves. These atmospheric waves can be tracked by the subtle  
48 brightness temperature changes they cause in the images. We show that the 1-min images used in  
49 our study capture finer details of the wave patterns and allow a better estimation of wave  
50 properties than the relatively infrequent full disk images. The high temporal frequency imagery  
51 also allows to determine the eruption sequence more precisely and reveal how the background  
52 winds affect the propagation of the waves.

## 53 **1 Introduction**

54 On 15 January 2022, the Hunga Tonga-Hunga Ha’apai submarine volcano ( $20.54^\circ\text{S}$ ,  
55  $175.38^\circ\text{W}$ , hereafter HTHH) experienced a climactic eruption which produced a plume with  
56 overshooting tops reaching record-setting altitudes of 55–57 km (Carr et al., 2022; Proud et al.,  
57 2022). The eruption generated worldwide tsunamis (Kubota et al., 2022; Purkis et al., 2023),  
58 lofted unprecedented amounts of water vapor directly into the stratosphere to heights of 30–40  
59 km (Khaykin et al., 2022; Millán et al. 2022; Randel et al., 2023), and perturbed the global  
60 electric circuit via extreme lightning activity (Bór et al., 2023).

61 Global seismic and microbarometer observations revealed that the eruption emitted a  
62 wide spectrum of acoustic and gravity waves, including audible sound, infrasound, and internal  
63 gravity waves (Matoza et al., 2022; Vergoz et al., 2022), which also caused significant changes  
64 in the ionosphere and thermosphere (Harding et al., 2022; Vadas et al., 2023a). Most prominent

65 among them was a large-amplitude Lamb wave, which circled the Earth several times (Amores  
66 et al., 2022; Heki, 2022; Otsuka, 2022; Wright et al., 2022).

67 The Lamb wave is a special acoustic wave that is hydrostatically balanced in the vertical  
68 direction and propagates in the horizontal direction only. The ideal Lamb wave is a mode of an  
69 isothermal and windless atmosphere, where it propagates non-dispersively and isotropically with  
70 a nominal sound speed of  $\sim 312 \text{ m s}^{-1}$  (Bretherton, 1969). A similar mode exists in the real  
71 atmosphere and travels as an edge wave guided by the surface with most of its energy  
72 concentrated in the troposphere (Garrett, 1969). Real Lamb waves do show dispersion and  
73 waveform distortion, whose magnitude depends mostly on the global winds and to a lesser  
74 degree on the vertical temperature structure and topography encountered along the travel path  
75 (Garrett, 1969; Sepúlveda et al., 2023). Under standard atmospheric conditions, the phase speed  
76 of Lamb waves can easily vary between  $294\text{--}319 \text{ m s}^{-1}$  (Garrett, 1969). Lamb waves propagate  
77 very efficiently because their attenuation distance largely exceeds the circumference of the Earth.  
78 They appear as a pseudo-mode bridging the gap between the acoustic and gravity modes and can  
79 exist at all periods ranging from a few minutes to about a day (Francis, 1973).

80 Several studies tracked the global propagation of the primary Lamb wave emitted by  
81 HTHH using infrared brightness temperatures from geostationary satellites (Amores et al., 2022;  
82 Matoza et al., 2022; Otsuka, 2022; Winn et al., 2023). All of these studies used full disk (FD)  
83 imagery available either at 10-min cadence from the Advanced Baseline Imager (ABI) aboard  
84 the Geostationary Operational Environmental Satellite-R series (GOES-R) and the Advanced  
85 Himawari Imager (AHI) aboard the Himawari-8 satellite or at 15-min cadence from the Spinning  
86 Enhanced Visible and Infrared Imager (SEVIRI) aboard the Meteosat Second Generation  
87 satellites. From such FD imagery, the horizontal phase speed, horizontal wavelength, and  
88 ground-based period of the Lamb wave were estimated as  $c_H \approx 303\text{--}323 \text{ m s}^{-1}$ ,  $\lambda_H \approx 400\text{--}500$   
89 km and  $\tau_R \approx 20\text{--}30 \text{ min}$ , respectively.

90 Studies analyzing surface pressure records or numerically simulating the atmospheric  
91 waves and the triggered meteotsunamis arrived at similar or even longer Lamb wavelengths and  
92 periods. The far-field envelope of the complex pressure wave packet can be roughly  
93 approximated by an  $N$ -wave or a positive triangular pulse of  $400\text{--}900 \text{ km}$  width and  $20\text{--}50 \text{ min}$   
94 duration (Heinrich et al., 2023; Kubota et al., 2022; Matoza et al., 2022; Vergoz et al., 2022;  
95 Watada et al., 2023; Winn et al., 2023).

96 In this study, we take advantage of the GOES-R mesoscale scans, which offer a limited-  
97 area ( $\sim 1,000 \times 1,000 \text{ km}^2$ ) view of the HTHH Lamb and gravity waves, but at an order of  
98 magnitude better temporal resolution of 1 min. We show that the long-period wave cannot be  
99 directly extracted from brightness temperature imagery against a highly varying background. The  
100 commonly used visualization technique of differencing image sequences characterizes instead  
101 the waveform time derivatives and thus constitutes a high-pass filter. Temporal aliasing due to a  
102 reduced sampling frequency, on the other hand, represents a compensating factor. As a result of  
103 these opposing effects, the FD difference imagery captures the long-period envelope of the full  
104 wave packet. However, it misses important high-frequency variations within the waveform,  
105 which can only be obtained from the mesoscale imagery.

106 The paper is organized as follows. Section 2 introduces the ABI mesoscale data. Section  
107 3 explains the emergence of the specific wave patterns that can be visualized in brightness  
108 temperature image differences. Section 4 analyzes the first two passages of the Lamb waves and

109 provides further examples of gravity waves captured in the high-resolution data. A discussion  
110 and conclusions are given in Section 5.

## 111 **2 ABI 1-minute mesoscale imagery**

### 112 2.1 Mesoscale domains

113 To identify and track atmospheric waves generated by the HTHH eruption, we used  
114 infrared (IR) imagery from ABI aboard GOES-17 (GOES-West) and GOES-16 (GOES-East).  
115 The vertical near-side perspective views of the Earth disk from the geostationary vantage points  
116 of GOES-17 and GOES-16 are depicted in Figures 1a and 1b, respectively. GOES-17, stationed  
117 at 137.2°W, observes the Pacific including HTHH, as well as Central and North America. The  
118 coverage area of GOES-16, stationed at 75.2°W, is centered on the Americas, but also includes  
119 the Eastern Pacific and parts of the Atlantic. The current ABI imaging Mode 6 scans the full disk  
120 every 10 minutes, the Pacific US (PACUS, GOES-17) and Continental US (CONUS, GOES-16)  
121 sectors every 5 minutes, and two mesoscale domains (M1, M2) per satellite every minute.

122 All previous studies used the 10-minute FD imagery for the global tracking of the main  
123 Lamb wave. The PACUS and CONUS scans offer an improved 5-minute temporal resolution  
124 over a  $\sim 5,000 \times 3,000$  km<sup>2</sup> sector covering the latitudes of the US (15°N–50°N). In this study,  
125 however, we exploit the mesoscale scans, which provide the highest cadence of 1 minute, albeit  
126 in a limited area.

127 A full disk IR image is given on a 5424×5424 fixed grid rectified to the Geodetic  
128 Reference System 1980 (GRS80) ellipsoid. The fixed grid has an angular sampling distance of  
129 56  $\mu$ rad, which corresponds to a spatial resolution of  $\sim 2$  km at the subsatellite point. A mesoscale  
130 domain is a 500×500-pixel square subset of an FD image, covering a  $\sim 1,000 \times 1,000$  km<sup>2</sup> area at  
131 the subsatellite point. Each mesoscale domain can be independently retargeted from its default  
132 position to follow evolving features of interest, such as severe weather or volcanic eruptions.

133 The ABI mesoscale domains were moved several times during 15–16 January 2022.  
134 Figure 1 shows, in chronological order, only those locations that were used for tracking the  
135 waves triggered by the eruptions. The GOES-17 M2 domain was centered on American Samoa  
136 to the northeast of HTHH between 02:41–05:59 UTC on 15 January. The midpoint and southern  
137 edge of this domain were respectively 930 km and 155 km from the volcano. Although this  
138 domain unfortunately missed the rising eruption column, it did however capture the earliest  
139 phases of wave propagation. In this domain, we used atmospheric surface pressure data collected  
140 in the National Park of American Samoa, Pago Pago (blue star in Figure 1) to explain the  
141 observed temperature anomaly waveform by the pressure anomaly waveform.

142 After a 1-hour gap, the GOES-17 M1 domain was centered on HTHH at 07:05 UTC on  
143 15 January and kept there for a little over 2 days. This domain observed the spreading of the  
144 stratospheric and near-tropopause plumes produced by the main eruption at  $\sim 04:29$  UTC and  
145 also captured the later smaller eruptions. These two domains provide a rich data source for the  
146 analysis of near-field wave phenomena.

147 The GOES-17 M2 domain was subsequently moved back to its default location over  
148 Alaska ( $\sim 9,000$  km from HTHH) and allowed the far-field observation of the A1 minor arc west-  
149 to-east wave passage between 11–14 UTC on 15 January. Additional far-field observations of the  
150 A1 wave passage over the southwest and southeast US were provided by the GOES-16 M2

151 domain (~9,500 km from HTHH) between 12–15 UTC and the GOES-16 M1 domain (~11,000  
152 km from HTHH) between 15–17 UTC on 15 January. Surface pressure data at Midland  
153 International Air and Space Port (Midland, Texas; red star in Figure 1) located in the GOES-16  
154 M1 domain was also analyzed.

155 The antipodal A2 major arc east-to-west wave passage on 16 January was first observed  
156 in the GOES-16 M2 domain, relocated to the southeastern US, and the GOES-16 M1 domain  
157 between 06–08 UTC. These two GOES-16 mesoscale domains cover nearly the same longitude  
158 range and half overlap with M2 being north of M1. The A2 wave passage was then imaged in the  
159 default GOES-17 M2 domain over Alaska between 08–11 UTC. Finally, the GOES-17 M1  
160 domain captured the confluence and interference of the returning A2 waves over HTHH between  
161 16:00–18:00 UTC.

162 Note that while the mesoscale scans are square images in the native fixed grid, they  
163 generally do not correspond to square areas in longitude-latitude space. As shown by the  
164 equirectangular projection in Figure 1c, the map distortion increases with increasing distance  
165 from the equatorial subsatellite point. As a result, the map distortion is largest for the default M2  
166 domain over Alaska, which is near the limb of the GOES-17 full disk (in fact, its top left  
167 northwestern corner contains space pixels). There is significant east-west stretching at such  
168 oblique view angles, especially poleward of 60°N.

169 A related caveat is that although the fixed grid is a regular grid in the satellite coordinate  
170 system with an angular spacing of 56  $\mu$ rad in both the east-west and north-south scan directions,  
171 it is an irregular grid in ellipsoid-projected distance. The nominal grid spacing (or ground  
172 resolution) is ~2 km only near the subsatellite point. Grid spacing generally increases with  
173 distance from the subsatellite point and shows significant variations within a given domain too.  
174 The horizontal distance between two neighboring image pixels is largest in the most obliquely-  
175 viewed GOES-17 M2 domain over Alaska, where it typically is in the range of 3–15 km. Grid  
176 spacing is finer in the rest of the domains, usually between 2.5–6.0 km. Therefore, when  
177 estimating the propagation speed of the observed waves, it is important to calculate ellipsoid-  
178 projected distances from the actual geodetic latitude and longitude of image pixels—we use the  
179 GRS80 ellipsoid.

## 180 2.2 Brightness temperatures

181 Spectral radiances were converted to the equivalent black body brightness temperature,  
182 henceforth simply brightness temperature (*BT*), as described in the *GOES R Series Product*  
183 *Definition and Users' Guide* (GOES-R PUG L1B Vol 3 Rev 2.2, 2019). We track waves directly  
184 in the fixed grid square images (500×500 pixels) to avoid unnecessary remapping and  
185 interpolation. The waves are detectable in all IR channels to a varying degree. For illustrations in  
186 this paper, we use C7, C9, C11, C12, or C13, choosing the one that provides the sharpest signal  
187 for a given time and location.

188 For the interpretation of the observed wave patterns, it is important to have at least a  
189 qualitative understanding of the altitude ranges the brightness temperatures represent. Out of the  
190 10 ABI IR channels, six are window channels (C7, C11, C13, C14, C15, C16) with a clear-sky  
191 vertical weighting (or contribution) function that peaks at the surface (Schmit et al., 2017). In  
192 these channels, a large portion of the signal originates from the surface in clear air, although  
193 water vapor, SO<sub>2</sub>, and CO<sub>2</sub> also modulate the *BT* to various degrees. In the presence of opaque

194 meteorological or volcanic clouds, however, the signal originates largely from the cloud altitude.  
195 In semitransparent clouds, there is still noticeable contribution from the surface and the *BT* is  
196 characteristic of an apparent height somewhere between the surface and cloud level.

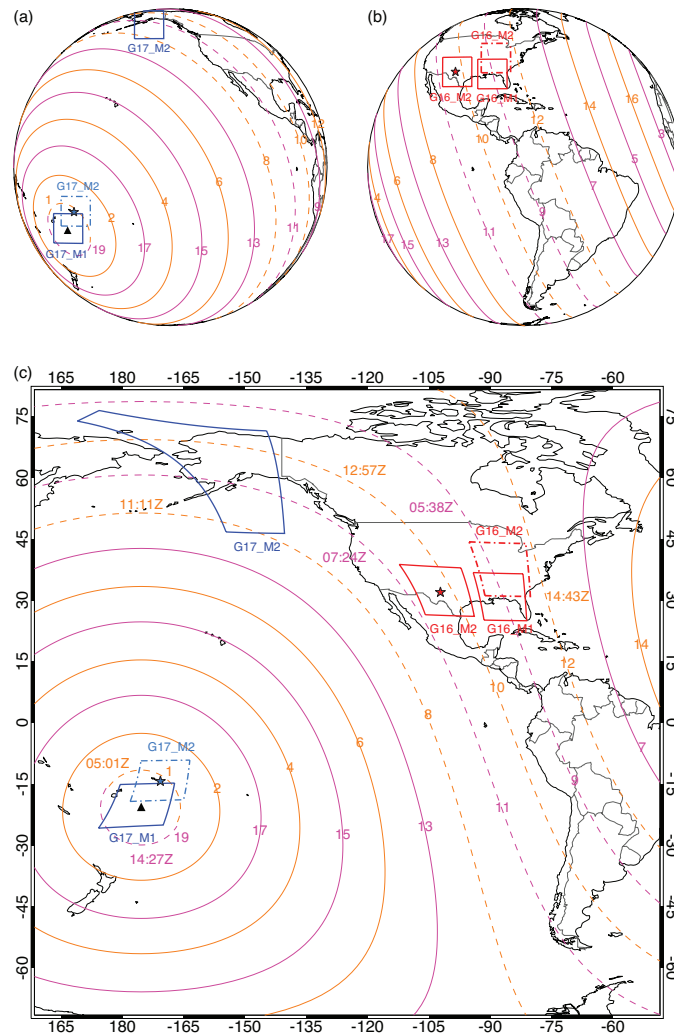
197 The clear-sky weighting function of the lower-, mid-, and upper-level water vapor  
198 channels (C10, C9, C8) peak at  $\sim 4$  km,  $\sim 6.5$  km, and  $\sim 8.2$  km altitude, respectively. Therefore,  
199 these channels are more representative of the mid to upper troposphere, although high-level  
200 clouds also affect the signal. Finally, the ‘ozone’ channel (C12) has a clear-sky weighting  
201 function with a peak at the surface as well as at  $\sim 22$  km altitude and, thus, characterizes the  
202 lower stratosphere (albeit water vapor absorbs in this channel too).

203 The vertical weighting functions are relatively broad and, hence, the clear-sky *BT*  
204 represents a weighted layer mean rather than a single level. Overall, the presence of a wave front  
205 in several IR channels and across different scene types is indicative of a vertically extensive and  
206 coherent wave.

207 We also note that the GOES-17 ABI suffered a loop heat pipe (LHP) anomaly, which prevents  
208 maintaining the IR detectors at their required temperatures during parts of the night under certain  
209 orbital conditions. After performance recovery steps, 97 % of imaging capability in the thermal  
210 infrared bands was regained (McCorkel et al., 2019); however, image degradation such as  
211 increased noise and striping are occasionally noticeable.

212

213  
 214  
 215  
 216  
 217  
 218  
 219  
 220  
 221  
 222  
 223  
 224  
 225  
 226  
 227  
 228



229 **Figure 1.** Geographic location of GOES-17 (G17, blue) and GOES-16 (G16, red) mesoscale  
 230 domains (M1, M2) used for wave tracking on 15–16 January 2022: **(a)** GOES-17 fixed grid  
 231 view, **(b)** GOES-16 fixed grid view, and **(c)** equirectangular projection. The black triangle is  
 232 HTHH. The blue and red stars mark the location of surface air pressure measurements at the  
 233 National Park of American Samoa and Midland International Air and Space Port, respectively.  
 234 The orange and magenta lines indicate isodistances ( $\times 1,000$  km) from the volcano and its  
 235 antipode, respectively. Arrival times at the dashed isodistances (orange - 15 January, magenta -  
 236 16 January) are derived using a nominal propagation speed of  $315 \text{ m s}^{-1}$  and the emission time of  
 237 the first detectable waves at 04:07 UTC on 15 January 2022. The temporal coverage of the  
 238 mesoscale domains is summarized in Table S1 in the Supporting Information.

239

### 240 3 Visualization of atmospheric waves

241 Differencing brightness temperature image sequences has been the main tool for the visualization  
 242 of the atmospheric waves generated by the eruption. In this section, we investigate which part of

243 the wave spectrum is in fact captured by such difference imagery.

### 244 3.1 The surface pressure waveform

245 Atmospheric pressure anomalies caused by the HTHH eruption were recorded all around  
246 the globe. Laboratory measurements and numerical simulations show that acoustic waveforms  
247 propagating through the atmosphere can get strongly distorted mostly by thermal  
248 inhomogeneities and turbulent wind velocity fluctuations (Averiyarov et al., 2011; Stout, 2018;  
249 Yuldashev, et al., 2017). Unlike the classic *N*-wave sonic boom, distorted waveforms can have  
250 rounded waves, several spikes, multiple shock fronts, and oscillations or even a maximum  
251 overpressure in the tail part. As a result, the observed HTHH Lamb wave packets are quite  
252 complex; nevertheless, their far-field envelopes can be roughly approximated by an *N*-wave or a  
253 positive triangular pulse (Matoza et al., 2022; Vergoz et al., 2022; Watada et al., 2023).

254 The amplitude of the pressure wave decreases with distance from the eruption, varying  
255 from  $\sim 30$  hPa in Tonga (64 km from HTHH) to  $\sim 0.5$  hPa in the far field (10k km from HTHH).  
256 The estimated duration (or ‘period’) of the enveloping pulse is between 20–50 min, which  
257 corresponds to a horizontal width (or ‘wavelength’) of 400–900 km for a phase velocity at the  
258 sound speed. The global propagation of this broad far-field atmospheric pressure pulse was well  
259 reproduced by Amores et al. (2022), who introduced an instantaneous sea level perturbation in a  
260 shallow water ocean model as well as by Watanabe et al. (2022), who imposed an instantaneous  
261 hot anomaly over the volcano in an atmospheric general circulation model. The atmospheric  
262 Lamb wave triggered a meteotsunami, the accurate numerical simulation of which also required  
263 the imposition of such long-period and long-wavelength pressure pulses as forcing (Heinrich et  
264 al., 2023; Kubota et al., 2022; Suzuki et al., 2023; Winn et al., 2023; Yamada et al., 2022).

265 For acoustic waves such as the Lamb wave, the temperature perturbations are in phase  
266 with and proportional to the pressure perturbations (Vadas, 2013). Therefore, the waveform of  
267 surface pressure anomalies approximates, to first order, the waveform of the brightness  
268 temperature anomalies embedded in the satellite images. The black curve in Figure 2a shows the  
269 surface pressure anomaly measured at the National Park of American Samoa (Pago Pago, Tutuila  
270 Island) between 04:00–06:00 UTC on 15 January (PurpleAir, 2023). The barometer provides  
271 measurements at a temporal resolution of  $\Delta t = 2$  min and is located  $\sim 850$  km from HTHH near  
272 the center of our G17\_M2 Samoa domain ( $14.27^\circ\text{S}$ ,  $170.70^\circ\text{W}$ ; blue star in Figure 1). This  
273 distance translates to a wave travel time of  $\sim 45$  min at the propagation speed of  $\sim 315$  m s<sup>-1</sup>  
274 derived in Section 4.1. The anomalies are given relative to the mean value of the 04:00–04:30  
275 UTC period (1006.5 hPa), when the pressure was very stable.

276 The first small pressure peak ( $\sim 0.3$  hPa) occurs at 04:52 UTC, corresponding to an  
277 emission time of  $\sim 04:07$  UTC at HTHH. Although this pressure anomaly is barely discernable, it  
278 likely is a real signal, because its emission time agrees with that of the very first visually  
279 detectable wave in our mesoscale *BT* imagery. Seismo-acoustic data (Matoza et al., 2022) and  
280 tsunami runup measurements in the Tonga Archipelago (Purkis et al., 2023) also indicate an  
281 explosive event at that emission time. In addition, Van Eaton et al. (2023) found a sudden  
282 increase in the plume’s width at 04:07 UTC using GOES-17 full disk visible images.

283

284

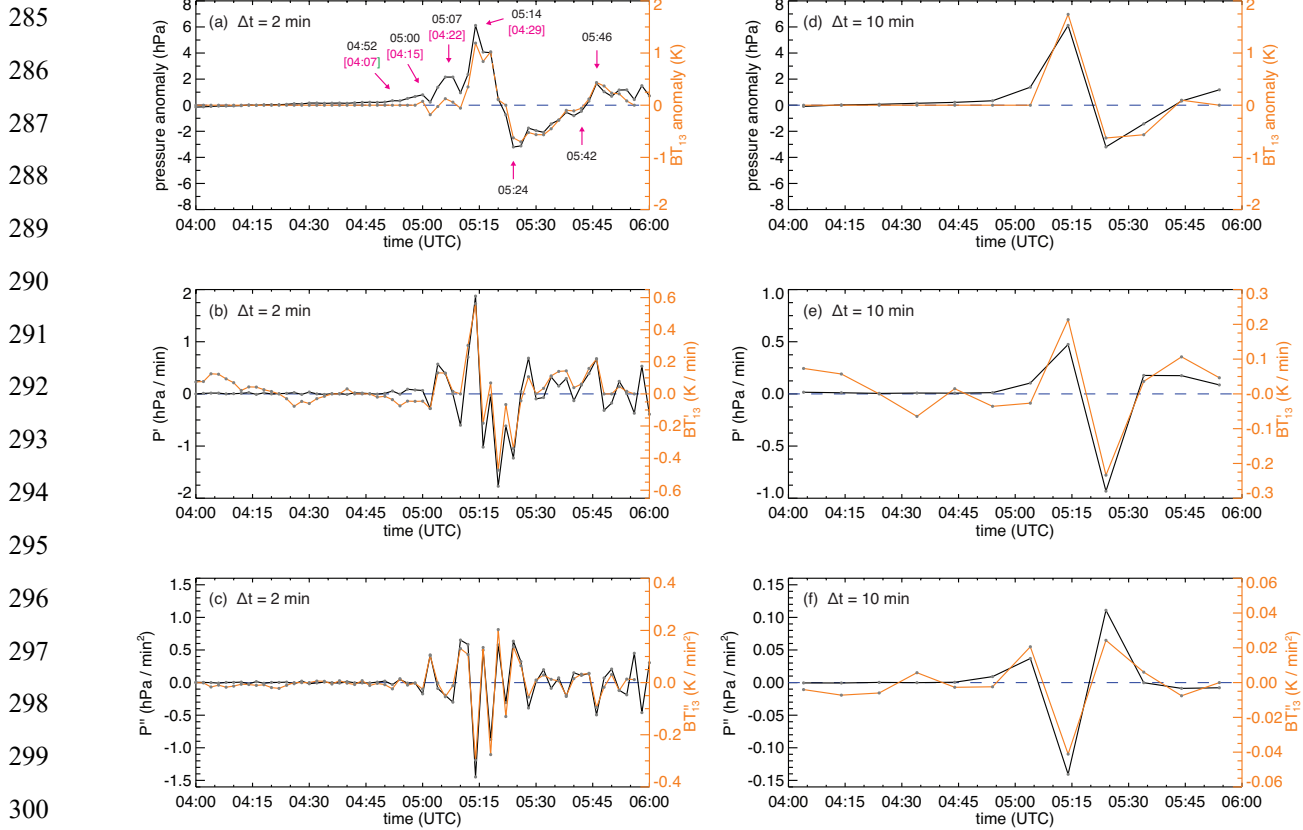


**Figure 2.** Atmospheric surface pressure ( $P$ , black) and channel 13 ( $10.3 \mu\text{m}$ ) brightness temperature ( $BT_{13}$ , orange) waveforms and their time derivatives at  $\Delta t = 2 \text{ min}$  sampling in Pago Pago, American Samoa between 04:00–06:00 UTC on 15 January 2022. **(a)** Pressure anomaly relative to the mean of the 04:00–04:30 period. The arrival times and the emission times (pink, in brackets) of individual pressure peaks are also indicated, assuming a propagation velocity of  $315 \text{ m s}^{-1}$ . The  $BT_{13}$  anomaly was reconstructed from the observed  $BT_{13}'$ . **(b)** The first time derivatives  $P'$  and  $BT_{13}'$ . **(c)** The second time derivatives  $P''$  and  $BT_{13}''$ . The time derivatives of  $BT_{13}$  were averaged along the isodistance of Pago Pago to reduce noise. Panels **(d)**, **(e)**, and **(f)** are the same as **(a)**, **(b)**, and **(c)**, respectively, but for  $\Delta t = 10 \text{ min}$ .

This minor anomaly is followed by two larger anomalies at 05:00 UTC ( $\sim 0.8 \text{ hPa}$ , emission time 04:15 UTC) and 05:07 UTC ( $\sim 2.1 \text{ hPa}$ , emission time 04:22 UTC). The peak overpressure of  $\sim 6.1 \text{ hPa}$  is recorded in Pago Pago at 05:14 UTC. The maximum HTHH plume-top height of 55–57 km was measured  $\sim 6 \text{ min}$  after the 04:29 UTC emission time of this main pressure pulse (Carr et al., 2022). Matoza et al. (2022) also report seismo-acoustic events with  $\sim 04:15 \text{ UTC}$  and  $\sim 04:30 \text{ UTC}$  emission times, while Purkis et al. (2023) claim an explosive blast with a  $\sim 04:18 \text{ UTC}$  emission time (in between the 2<sup>nd</sup> and 3<sup>rd</sup> peak in our pressure data).

The pressure quickly drops in the next 10 min, reaching its lowest value, a  $-3.2 \text{ hPa}$  anomaly, at 05:24 UTC. Thus, the amplitude of the main explosion is  $\sim 9.3 \text{ hPa}$  in Samoa. The pressure then recovers with some fluctuations by 05:42 UTC and shows a smaller trailing peak ( $\sim 1.7 \text{ hPa}$ ) at 05:46 UTC.

323 The full wave packet is a combination of four consecutive explosions of increasing  
324 magnitude. A range of characteristic time spans can be derived, depending on whether one  
325 focuses on the main blast or the full packet. Extrapolating backward and forward in time from  
326 the primary pressure peak and trough, the main blast can be approximated by an  $N$ -wave starting  
327 at  $\sim 05:08$  UTC and ending at  $\sim 05:32$  UTC. This  $N$ -wave has a rise time of 6–8 min and a total  
328 duration of  $\sim 24$  min. The time difference between the primary peak and the first trailing peak  
329 yields a slightly longer period of  $\sim 32$  min. The duration of the full wave packet is  $\sim 50$  min  
330 (04:52–05:42 UTC), comprising a  $\sim 28$ -min positive phase and a  $\sim 22$ -min negative phase. This  
331 range of time span estimates agrees with that reported in previous studies.

332 Figure S1 in the Supporting Information plots 1-min barometer readings (Joe LaPlante,  
333 personal communication) collected at nearby Coconut Point (Nu'uuli, Tutuila Island), which  
334 show essentially the same pressure waveform comprising of the main pulse and at least two  
335 preceding smaller pulses. Although this data has better temporal resolution, its quantization  
336 ( $\Delta p = 0.34$  hPa) is significantly coarser than that of the 2-min pressure measurements ( $\Delta p =$   
337  $0.01$  hPa); hence, we use the latter to calculate waveform derivatives in the next section. Figure  
338 S1 also plots 1-min surface pressures at Midland International Air and Space Port (close to the  
339 center of the G16\_M2 Texas domain; red star in Figure 1) obtained from the Automated Surface  
340 Observing System (ASOS, 2023). This far-field waveform ( $\sim 9,716$  km or  $\sim 8.5$  hr from HTHH)  
341 is very similar to the near-field ones in Samoa, demonstrating the stability of the shock wave as it  
342 traversed the globe, but its amplitude is an order of magnitude smaller,  $\sim 0.9$  hPa.

343 The black curve in Figure 2d demonstrates how the observed waveform changes when  
344 the  $\Delta t = 10$  min cadence of full disk imagery is used. Here the 2-min pressure time series is  
345 subsampled backward and forward in time from 05:14 UTC to preserve the main peak. The  
346 smaller blasts and other fine details are indistinguishable and all that remains is the  $\sim 50$ -min  
347 envelope of the full wave packet. As chance would have it, the rise time and the time span of the  
348 peak-to-trough drop of the central  $N$ -wave are both close to 10 min; hence, the primary Lamb  
349 pulse is well represented even at the reduced FD sampling.

### 350 3.2 Waveform time derivatives

351 Visualizing the HTHH-induced temperature perturbations in raw  $BT$  imagery is rather  
352 problematic. The amplitude of the temperature variations rapidly decreases with distance and at  
353 most represents a signal of a couple of percent. Pressure perturbations have a similar relative  
354 magnitude, but they are superimposed on a fairly homogeneous and steady background. The  
355 temperature perturbations, in contrast, are superimposed on a heterogeneous and rapidly varying  
356 background. Spatiotemporal variations in clouds (advection, growth, dissipation) and to a lesser  
357 degree in water vapor and trace gases lead to a challenging background scene for the  
358 identification and tracking of faint wavelike features. The large dynamic range of  $BT$  makes it  
359 difficult to achieve enough local contrast both in cold (bright, cloudy) and warm (dark, clear sky)  
360 areas when tone mapping the image.

361 Waves are easier to detect in the time derivatives of the brightness temperature. For each  
362 pixel, we approximate the first time derivative of  $BT$  at time  $t$  using a backward finite-difference  
363 scheme

364

365 
$$BT' = \frac{BT(t) - BT(t - \Delta t)}{\Delta t} \quad (1)$$

366

367 and the second time derivative using a second-order central finite-difference scheme

368

369 
$$BT'' = \frac{BT(t + \Delta t) - 2BT(t) + BT(t - \Delta t)}{\Delta t^2}, \quad (2)$$

370

371 where  $\Delta t$  is the time difference between the images. Apart from a scaling factor, the first time  
 372 derivative is just the difference between two subsequent images, while the second time derivative  
 373 is the difference between the mean of three subsequent images and the central image of the  
 374 triplet.

375 The mesoscale images are available at a time resolution of  $\Delta t = 1$  min. However, with a  
 376 subsampling rate of  $n > 1$ , that is, selecting only every  $n$ th image from the sequence, we can  
 377 investigate the spatiotemporal aliasing effect of longer sampling periods on the appearance of  
 378 wave patterns. For example, a sampling period of  $\Delta t = 10$  min mimics the GOES-R and  
 379 Himawari-8 full-disk images that were used in previous studies.

380 It is important to note that these (discrete) time derivatives act as high pass filters, where  
 381 higher frequencies get larger weights than lower frequencies. Before considering  $BT$  images, we  
 382 first demonstrate the effect of the time differentiators on the pressure waveform, which is a proxy  
 383 for the temperature waveform. The black curves in Figure 2b and Figure 2c plot the first  
 384 derivative ( $P'$ ) and second derivative ( $P''$ ) of the Samoa pressure time series ( $\Delta t = 2$  min),  
 385 respectively. These can be thought of as the pressure (or  $BT$ ) waveform derivatives at the image  
 386 pixel which corresponds to the barometer's location. As shown, the differentiators emphasize the  
 387 shorter period variations within the waveform rather than the long-period envelope of the full  
 388 wave packet. The first time derivative is the pressure tendency, which characterizes the local  
 389 steepness of the waveform. The second derivative describes the local concavity of the graph: the  
 390 waveform is concave up (or convex) if  $P'' > 0$  and concave down if  $P'' < 0$ .

391 The derivative of the waveform is frequently used in laboratory investigations of  $N$ -  
 392 waves, especially ones with multiple shocks similar to the HTHH pressure wave. For example,  
 393 the peak overpressure and the rise time are difficult to evaluate in distorted waveforms found in  
 394 turbulent flow. These important acoustic wave parameters can be better defined based on the first  
 395 derivative of the pressure waveform (Averiyanov et al., 2011; Yuldashev, et al., 2017).  
 396 Analyzing  $P'$  allows ranking shocks by strength (steepness), separating close shocks that  
 397 otherwise might be considered as one long shock, and enables detecting shocks in the tail part of  
 398 the packet.

399 The first and second derivatives of the pressure waveform sampled at the reduced FD rate  
 400 of  $\Delta t = 10$  min are given by the black curves in Figures 2e and 2f, respectively. In both cases,  
 401 the maxima of the derivatives are separated by 20 min. By chance, this time span agrees well

402 with the  $\sim 24$  min duration of the  $N$ -wave that can be fitted to the primary Lamb pulse of the full  
403 wave packet.

### 404 3.3 Image processing

#### 405 3.3.1 Gray scaling, smoothing, contrast enhancement

406 Although it high pass filters the data, the major advantage of taking the time derivatives  
407 of  $BT$  is that it largely eliminates the high dynamic-range background image comprising a  
408 mixture of clear (warm) and cloudy (cold) areas. In the significantly reduced dynamic range  $BT$   
409 derivatives, it is easier to achieve good local contrast throughout the entire scene. The time  
410 derivatives are first scaled to 256 gray levels using an appropriate initial range, e.g.,  $\pm 1$  K  $\text{min}^{-1}$   
411 for  $BT'$  and  $\pm 0.25$  K  $\text{min}^{-2}$  for  $BT''$ . The images are then histogram equalized. Because this  
412 means a palette change for each image, we omit the colorbar in the figures and animations. , For  
413 the visualization of wave fronts, however, spatial coherence is more important than pixel  
414 intensity (the magnitude of the time derivative). Histogram equalization readjusts the intensities  
415 and allows areas of lower local contrast to gain a higher contrast. In the resulting images, the  
416 bright wave crests and dark troughs respectively correspond to the maxima and minima of the  
417 waveform derivatives plotted in Figure 2.

418 The images are also smoothed with a moving average boxcar filter. The smallest  
419 averaging window of  $3 \times 3$  pixels is already adequate, but in this study, we opt for a slightly larger  
420  $5 \times 5$ -pixel window, which in our experience leads to a clearer separation of wave fronts. Mean  
421 filtering is applied in all cases, except in the analysis of the shortest wavelength ( $\sim 15$  km) gravity  
422 waves, where the crests and troughs already show good contrast in the unfiltered images and  
423 smoothing would unnecessarily bias the results (see Section 4.2.1). As an example, Figure 3  
424 compares the highest temporal resolution ( $\Delta t = 1$  min) first and second time derivatives of  
425 channel 11 ( $8.4 \mu\text{m}$ )  $BT_{11}$  for a sunset scene in the GOES-17 M2 Samoa domain. The channel 2  
426 ( $0.65 \mu\text{m}$ ) visible radiances and  $BT_{11}$  itself are also plotted for context in Figures 3a and 3b,  
427 respectively. Most of the domain is covered with clouds, ranging from low-level ones to deep  
428 convection. In the bottom left corner of Figure 3a, the stratospheric plume from the main  
429 eruption intrudes into the domain and casts a shadow on lower-level clouds. The right and  
430 bottom third of the domain are warm ocean peppered only with small popcorn cumuli and,  
431 hence, show high  $BT_{11}$  (black areas in Figure 3b).

432

433

434

435

436

437

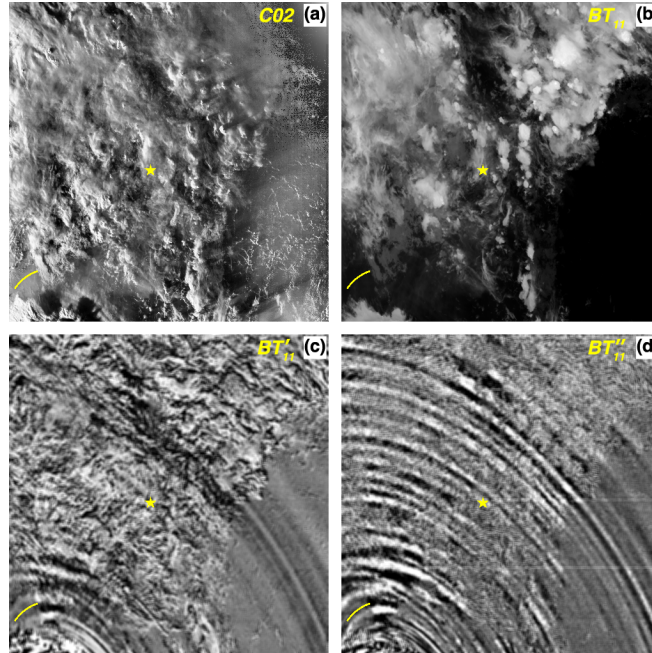
438

439

440

441

442  
443  
444  
445  
446  
447  
448  
449  
450  
451  
452  
453  
454



455 **Figure 3.** (a) Channel 2 ( $0.65\ \mu\text{m}$ ) visible radiances, (b) channel 11 ( $8.4\ \mu\text{m}$ ) brightness  
456 temperatures  $BT_{11}$ , (c) first time derivative  $BT'_{11}$ , and (d) second time derivative  $BT''_{11}$  in  
457 G17\_M2 (Samoa) at 05:35 UTC on 15 January 2022. The visible image was enhanced by  
458 adaptive histogram equalization and  $BT_{11}$  was gray scaled between 190K (white) and 290K  
459 (black). The interval used for calculating the time derivatives is  $\Delta t = 1\ \text{min}$ . The time derivative  
460 images were gray scaled over the respective ranges of  $\pm 1\ \text{K min}^{-1}$  and  $\pm 0.25\ \text{K min}^{-2}$ , histogram  
461 equalized, and mean filtered using a  $5\times 5$ -pixel window. The yellow star marks the location of the  
462 Pago Pago pressure time series plotted in Figure 2. The yellow arc in the bottom left are clear  
463 pixels  $\sim 341\pm 2\ \text{km}$  from HTHH with a backazimuth of  $320^\circ\text{--}345^\circ$ , the mean brightness  
464 temperature of which is plotted in Figure 5.

465

466 The concentric arcs of waves emanating from HTHH are partially visible in  $BT'_{11}$ ,  
467 especially over mostly clear ocean (Figure 3c). However, the waves are still difficult to discern  
468 in thicker clouds, where large temperature fluctuations due to horizontal or vertical cloud motion  
469 mask the small eruptive temperature anomalies. This complicating background is greatly  
470 diminished in  $BT''_{11}$ , which enhances the spatially coherent signal from fast propagating waves  
471 (Figure 3d). The second time derivative collates information from three images and, thus, works  
472 better than the first time derivative, which is based on two images. The  $BT''_{11}$  field reveals a  
473 multitude of closely spaced wave crests and troughs, even in cloudy areas. Due to its obvious  
474 superiority, we use the second time derivative of brightness temperatures for most subsequent  
475 analysis.

476

477 The emergent pattern of alternating brighter and darker arcs is insensitive to the type of  
478 finite difference scheme. Replacing the central differences in Equation 2 with forward or  
479 backward differences leads to a pattern that is shifted slightly forward or backward in the radial  
direction, but otherwise shows the same fine-scale band structure.

480 The concentric waves in Figure 3d can be easily followed from clear ocean over to high-  
481 level clouds without a noticeable dislocation in the arcs at the clear-cloudy interface and are also  
482 present in all IR channels, pointing to Lamb waves that span the full depth of the troposphere.  
483 Channel differences are further demonstrated in the Supporting Information (Figures S2 and S3).

484 Of the earlier studies, Wright et al. (2022) used the first time derivative, while Amores et  
485 al. (2022), Matoza et al. (2022), Otsuka (2022), and Winn et al. (2023) used the second time  
486 derivative of brightness temperatures to identify waves. However, all previous studies were  
487 based on full-disk imagery with a significantly longer sampling period of  $\Delta t = 10$  min for  
488 GOES-R and Himawari-8 and  $\Delta t = 15$  min for Meteosat. The consequences of such reduced  
489 temporal sampling are discussed in Section 3.6.

### 490 3.3.2 Spatial Fourier filtering

491 Although the used boxcar averaging already constitutes a low-pass spatial filter,  
492 additional spatial filtering can be applied to the data to improve the detection of the dominant  
493 wave signature. The  $BT''$  images are converted by a fast Fourier transform (FFT) into the  
494 frequency domain, in which an ellipsoidal filter removes certain high-wavenumber components  
495 and then the result is transformed back into the spatial domain by the inverse FFT.

496 Figure 4 demonstrates FFT filters for the two main wave pattern types encountered in the  
497 mesoscale observations. In near-field domains, the dominant pattern consists of concentric  
498 circles or arcs (Figure 4a). Here we note that the vertical near-side perspective view (fixed grid  
499 image) is a non-conformal projection in which angles and shapes are distorted; thus, circles  
500 appear as ellipses away from the subsatellite point. In far-field domains, the characteristic pattern  
501 is a train of bands, whose orientation (slope) depends on the domain's geographic location  
502 relative to HTHH (Figure 4d).

503 The 2D spatial power spectrum (Figures 4b and 4e) is zeroed outside of an ellipsoidal  
504 mask to reduce high-frequency variations, noise, and striping. Instead of using a fixed mask, we  
505 subjectively adjust the size and rotation of the ellipse per domain, such that it emphasizes the  
506 dominant wave patterns (Figures 4c and 4f). The animations given in the Supporting Information  
507 demonstrate the filter adjustment.

508 In our experience, low-pass FFT filtering might not significantly enhance the visual  
509 perception of waves in individual static images. Nevertheless, it always helps detecting the  
510 passage of waves and estimating their phase speed in the time–distance plots (or keograms) we  
511 introduce in Section 4.1.

512

513

514

515

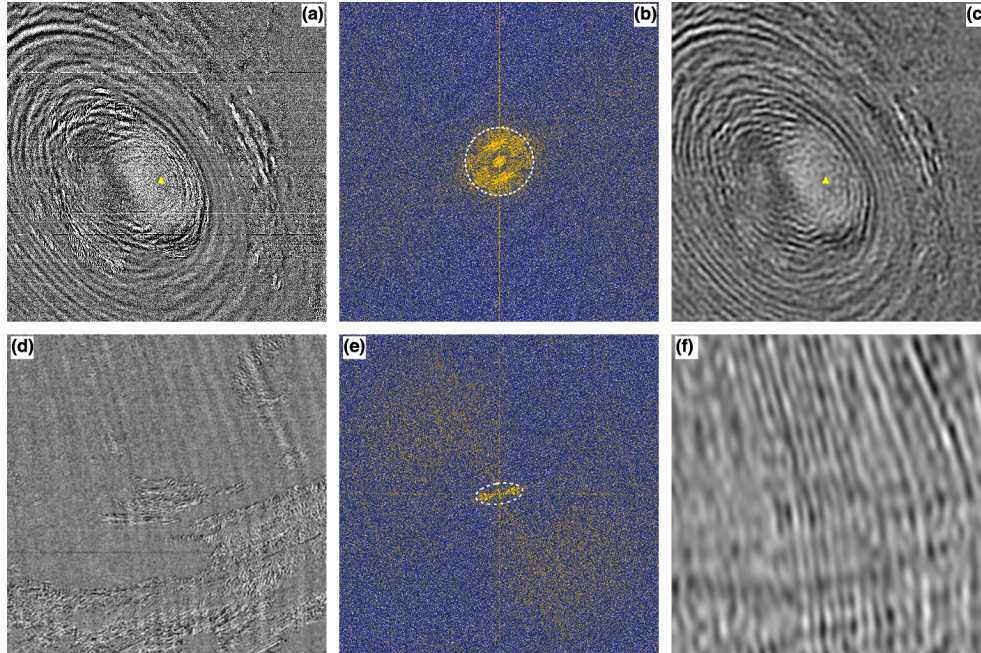
516

517

518

519

520  
521  
522  
523  
524  
525  
526  
527  
528  
529  
530  
531  
532



533 **Figure 4.** Examples of low-pass FFT filtering of  $BT''_{12}$  ( $9.6 \mu\text{m}$ ): **(top row)** concentric circles in  
534 the near-field G17\_M1 HTHH domain (HTHH marked by the yellow triangle) at 07:15 UTC on  
535 15 January 2022 and **(bottom row)** meridional bands in the far-field G16\_M2 domain (Texas) at  
536 13:35 UTC on 15 January 2022. The interval used for calculating the time derivative is  $\Delta t = 1$   
537 min. **(a, d)** Raw grayscale image. **(b, e)** Log of the 2D spatial power spectrum. The filter only  
538 keeps frequencies within the white dashed circle/ellipse. **(c, f)** Spatial frequency-filtered image.  
539

### 540 3.4 The primary Lamb wave in $BT$

541 As discussed earlier, detecting the HTHH-induced absolute temperature perturbations on  
542 a pixel-by-pixel basis is difficult, because the typical spatiotemporal variations in  $BT$  due to  
543 tropospheric dynamics usually mask the signal. However, it is possible to extract the mean  
544 signature of the long-period primary wave in certain cloud-free areas, where the background  
545 temperature remains relatively steady without large fluctuations. The yellow arc in Figure 3  
546 marks such a set of mostly clear pixels, which are  $\sim 341 \pm 2$  km from HTHH with a backazimuth  
547 of  $320^\circ$ – $345^\circ$ . Assuming a wave velocity of  $\sim 315 \text{ m s}^{-1}$ , these pixels are  $\sim 18$  min downstream  
548 from HTHH and  $\sim 26$  min upstream from Pago Pago (indicated by the yellow star).

549 Figure 5a plots the 1-min resolution temporal variation of the mean  $BT_{12}$  over the arc  
550 between 03:58–05:58 UTC. We use the ozone channel 12, because it is less sensitive to clouds  
551 due to its weighting function peaking in the stratosphere. A wave with an amplitude of  $\sim 5\text{K}$  and  
552 period of  $\sim 30$  min is apparent in the mean temperature. The 04:51 UTC and 05:20 UTC maxima  
553 in the mean  $BT_{12}$  correspond to the 05:14 UTC and 05:46 UTC pressure peaks measured  
554 downstream in Pago Pago (see Figure 2a).

555 A similar  $\sim 30$  min-period temperature variation corresponding to the main Lamb pulse is  
556 also detectable in the far-field G16\_M2 Texas domain. Figure 5b depicts the temporal variation

557 of  $BT_{12}$  averaged over a subset of clear pixels ( $\sim 9,974 \pm 2$  km from HTHH with a backazimuth of  
 558  $49^\circ$ – $54^\circ$ ) between 12:00–14:00 UTC. Here the HTHH-induced temperature perturbations are  
 559 superimposed on a generally decreasing background  $BT$  and have an order of magnitude smaller  
 560 amplitude of only  $\sim 0.3$ K.

561

562

563

564

565

566

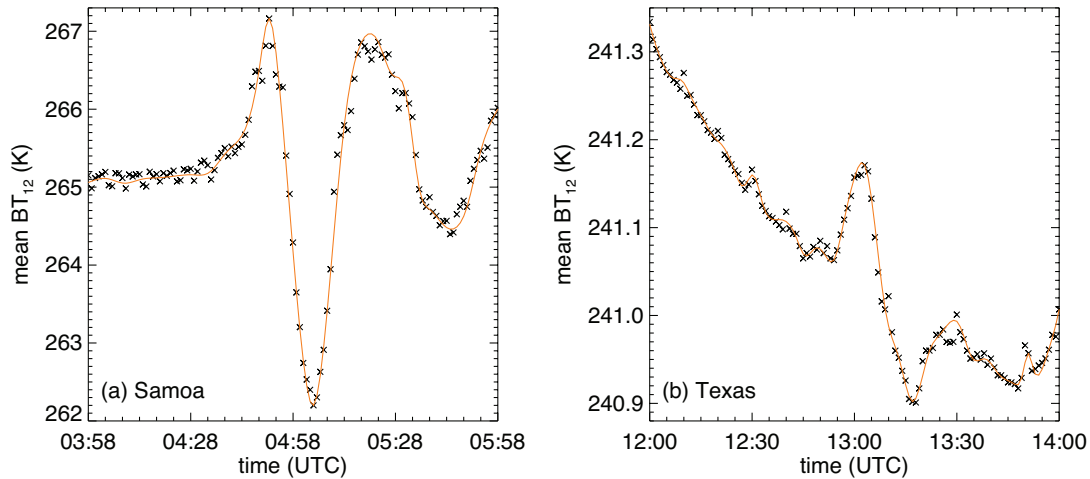
567

568

569

570

571



572 **Figure 5.** Time series of mean  $BT_{12}$  calculated for a set of clear pixels in **(a)** G17\_M2 Samoa  
 573 domain (yellow arc in Figure 3) and **(b)** G16\_M2 Texas domain (pixels  $\sim 9,974 \pm 2$  km from  
 574 HTHH with a backazimuth of  $49^\circ$ – $54^\circ$ ). The orange cubic spline fit is plotted merely as visual  
 575 guide.

576

### 577 3.5 A simple model of the temperature wave packet

578 As discussed previously, the pressure waveform can be used as a first-order model of the  
 579 temperature waveform, especially in the nearest Samoa domain, where the pressure signal is  
 580 robust. We devise temperature anomalies by linearly scaling the 2-min pressure anomalies in  
 581 Figure 2a such that the peak-to-trough amplitude becomes 2K (+1.3K at 05:14 UTC and -0.7K at  
 582 05:24 UTC). The amplitude of the temperature anomaly generally decreases with distance from  
 583 HTHH and also depends on altitude and channel. We show later that the amplitude of the mean  
 584 temperature anomaly reconstructed from the observed window channel  $BT$  time derivatives is  
 585  $\sim 2$ K at the isodistance of Pago Pago. Such a  $BT$  perturbation is representative of the cloudy  
 586 regions dominating our scene, but it is an overestimate in clear sky regions. In the latter, the  
 587 peak-to-trough temperature amplitude is only 0.5–1.0K, as estimated by Otsuka (2022) for an  
 588 isothermal atmosphere and adiabatic pressure change.

589 This synthetic cloud-level temperature waveform  $T_p$  is propagated through the G17\_M2  
 590 Samoa domain assuming isotropic spreading with a speed of  $315 \text{ m s}^{-1}$ . The waveform  
 591 derivatives are then calculated and processed as described in Sections 3.2 and 3.3.

592 Movie S1 in the Supporting Information shows the propagation of the modeled  
 593 temperature anomaly waveform and its derivatives between 03:58–05:58 UTC. Snapshots  
 594 corresponding to the passage of the maximum positive and negative temperature anomaly over

595 Pago Pago are plotted in Figure 6.

596 At 05:14 UTC, the broad bright band in the  $T_p$  image along Pago Pago's isodistance (850  
597 km) represents the primary peak of the wave packet (Figure 6a). The two fainter bands  
598 downstream correspond to the two smaller preceding peaks of the waveform. The darkest band  
599 ~200 km upstream (650 km isodistance) is the trough of the main Lamb pulse, which reaches  
600 Pago Pago at 05:24 UTC (Figure 6d). The full ~50 min wave packet is confined between the  
601 250–1,250 km isodistances in Figure 6a and between the 450–1,450 km isodistances in Figure 6d  
602 (the packet moves ~190 km per 10 min).

603

604

605

606

607

608

609

610

611

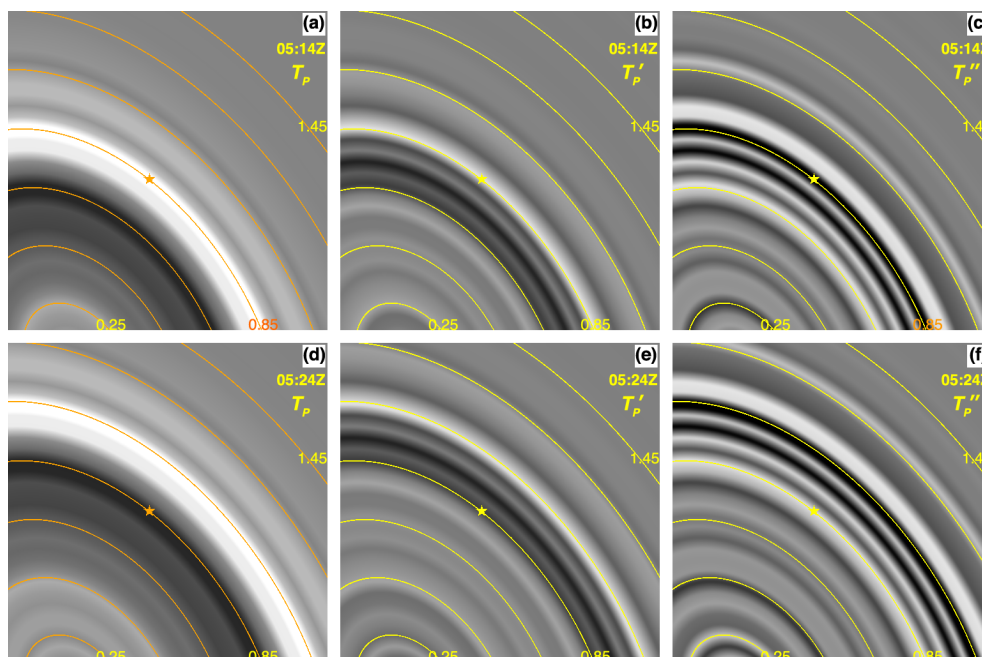
612

613

614

615

616



617 **Figure 6.** Temperature anomaly waveform and its time derivatives modeled on the Pago Pago  
618 pressure anomaly waveform and propagated through the G17\_M2 Samoa domain, at (**top row**)  
619 05:14 UTC and (**bottom row**) 05:24 UTC on 15 January 2022. (**a, d**) Temperature anomaly  $T_p$   
620 gray scaled between  $\pm 1\text{K}$  (white to black). (**b, e**) First derivative  $T'_p$ . (**c, f**) Second derivative  $T''_p$ .  
621 The star marks Pago Pago and the orange or yellow lines are isodistances ( $\times 1,000$  km) from  
622 HTHH drawn at 200 km intervals.

623

624 The first derivative of the temperature perturbations  $T'_p$  shows a larger number of thinner  
625 bands, as it highlights the temperature tendency within the packet. The bright band along Pago  
626 Pago's isodistance at 05:14 UTC marks the largest temperature increase at the peak of the main  
627 pulse (Figure 6b). In contrast, the dark band passing Pago Pago 10 min later represents the  
628 steepest temperature drop at the trough of the main pulse (Figure 6e). The broad long-period  
629 variation in temperature, however, cannot be identified in this representation.

630

631 The second derivative of the temperature perturbations  $T''_p$  visualizes the fine-scale  
632 variations the sharpest, as it represents the local concavity of the waveform. Its sign is usually  
opposite of  $T'_p$  for our particular waveform. Along Pago Pago's isodistance,  $T''_p$  is negative at

633 05:14 UTC (dark band in Figure 6c) and positive at 05:24 UTC (bright band in Figure 6f),  
 634 because the waveform is concave down near the peak and concave up near the trough of the  
 635 main Lamb pulse. The long-period temperature variation is not visually encoded in  $T_P''$  either,  
 636 because concavity is generally uncorrelated with the magnitude of the temperature anomaly.

637 In real world data, the temperature waveform is superimposed on a spatiotemporally  
 638 highly variable background. To mimic this, we simply add the modeled temperature perturbation  
 639  $T_P$  to actual  $BT_{11}$  imagery obtained before the eruption. Recall that mesoscale imagery in the  
 640 G17\_M2 Samoa domain is available between 02:41–05:59 UTC on 15 January and the first  
 641 visually detectable wave only appears at 04:16 UTC. Thus, imagery prior to 04:16 UTC do not  
 642 contain the HTHH wave signature and can be safely combined with the  $T_P$  shown in Figure 6.

643 Movie S2 in the Supporting Information shows such ‘simulated’ cloudy  $BT_{11}$  imagery, its  
 644 second time derivative, as well as the second time derivative of the actually observed  $BT_{11}$ . The  
 645 05:14 UTC and 05:24 UTC snapshots of the simulated and observed waveform derivatives are  
 646 plotted in Figure 7. Note that the cloud patterns are at slightly different locations in the simulated  
 647 and observed images, because the former depicts the cloud field at an earlier time than the latter.

648

649

650

651

652

653

654

655

656

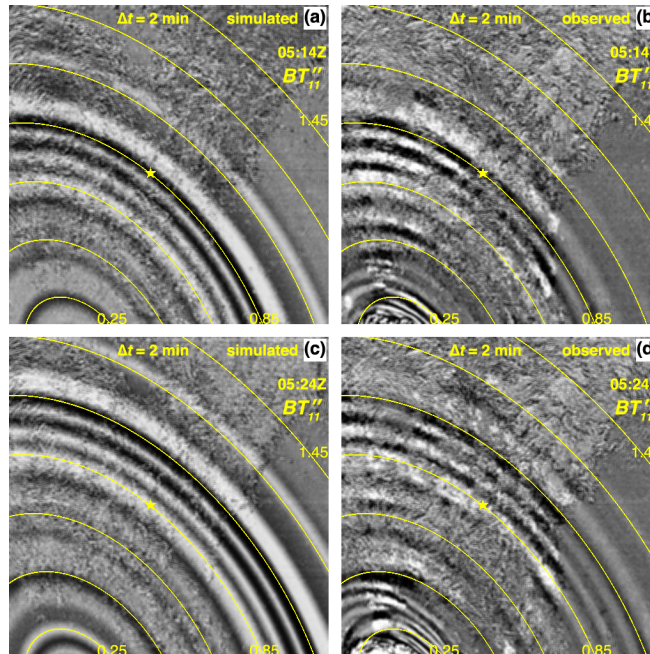
657

658

659

660

661



662 **Figure 7.** Second time derivative  $BT_{11}''$  visualized against a cloudy background: (a, c) simulated  
 663 and (b, d) observed in the G17\_M2 Samoa domain at (top row) 05:14 UTC and (bottom row)  
 664 05:24 UTC on 15 January 2022. The simulated images combine the modeled temperature  
 665 anomalies in Figure 6 with pre-eruption  $BT_{11}$  images that were obtained 77 min earlier than the  
 666 actual observation time of the waves indicated in the panels. The star marks Pago Pago and the  
 667 yellow lines are isodistances ( $\times 1,000$  km) from HTHH drawn at 200 km intervals.

668

669

670

Unlike against a uniform background as in Figure 6, the passage of the temperature  
 perturbations cannot be discerned against a natural cloudy background (see Movie S2). The

671 second derivative of the simulated brightness temperatures, however, well describes that of the  
 672 observed ones. The sequence, width, and location of the bright and dark arcs of the observed and  
 673 simulated waveform derivatives are in excellent agreement—the contrast variations of the  
 674 simulated patterns are, however, overemphasized in clear sky areas, because the imposed cloud-  
 675 level temperature anomalies are excessive in cloud-free regions. The only exception is the  
 676 bottom left corner of the domain, where the observations show a larger number of shorter period  
 677 wave fronts. It is here where the stratospheric umbrella of the HTHH plume intrudes the domain  
 678 and hence the satellite observations are likely dominated by gravity waves. Unlike Lamb waves,  
 679 which extend through the entire troposphere, these high-altitude gravity waves cause no  
 680 measurable anomalies in the Pago Pago surface pressure on which our assumed temperature  
 681 perturbations are based; thus, gravity waves are missing from the simulated images.

682 As demonstrated, the pressure perturbations explain the salient features of the  
 683 temperature waveform derivatives visualized in the satellite imagery. The relationship between  
 684 the pressure and temperature perturbations, however, can be further quantified. The orange  
 685 curves in Figures 2b and 2c depict the observed (real) temporal variation of the first and second  
 686 derivative of  $BT_{13}$  at Pago Pago—here the temperature derivatives were averaged along the 850-  
 687 km isodistance to reduce noise. The temperature and pressure waveform derivatives match up  
 688 excellently. The correlation between  $P'$  and  $BT'_{13}$  is 0.9 and that between  $P''$  and  $BT''_{13}$  is 0.94 for  
 689 the entire two-hour period. The slightly lower correlation between the first derivatives is due to  
 690 natural temperature variations in the 4–5 UTC period before the arrival of the eruption's pressure  
 691 wave. In the post-arrival period of 5–6 UTC, both the first and second derivatives correlate at  
 692 0.94.

693 Finally, the temperature perturbations can be approximately reconstructed from the  
 694 measured  $BT$  time derivatives by recursively applying the inverse of the finite difference  
 695 operators in Equations 1 and 2 (antidifference operator). The reconstruction is unique up to an  
 696 additive constant when using the first derivatives and up to an additive linear trend when using  
 697 the second derivatives.

698 The orange curve in Figure 2a depicts the  $BT_{13}$  anomalies reconstructed from the mean  
 699  $BT''_{13}$  plotted in Figure 2c. Here, we started the recursion at 5 UTC and removed a linear trend  
 700 from the reconstructed temperature anomalies—the observed mean  $BT_{13}$  for Pago Pago's  
 701 isodistance also increased between 5–6 UTC, unrelated to the eruption. As shown, the  
 702 reconstructed mean temperature anomaly waveform has a peak-to-trough amplitude of  $\sim 2$ K and  
 703 correlates well with the observed surface pressure waveform with a coefficient of 0.94.

704 The corresponding results for  $\Delta t = 10$  min sampling are given in Figures 2d, 2e, 2f and  
 705 Figure 8. Both time derivatives of the subsampled temperature waveform show the familiar  
 706 positive–negative–positive anomaly pattern of the main Lamb pulse found by previous studies  
 707 using FD imagery. There is a slight asymmetry between the positive peaks. The first peak is  
 708 larger and narrower than the second one for the first derivative, while the opposite is true for the  
 709 second derivative where the second peak is somewhat larger.

710 In FD imagery, these subsampled waveform derivatives manifest as bright–dark–bright bands of  
 711  $\sim 190$ – $200$  km width (the distance the acoustic wave packet travels in 10 min). Depending on the  
 712 relative magnitude of the positive peaks, the cloud background, as well as the applied spatial  
 713 smoothing and color saturation, sometimes only the single bright band of the larger peak is  
 714 discernable. As before, the differences between the simulated and observed patterns in the

715 bottom left corner of the domain are likely due to gravity waves in the stratospheric umbrella.

716

717

718

719

720

721

722

723

724

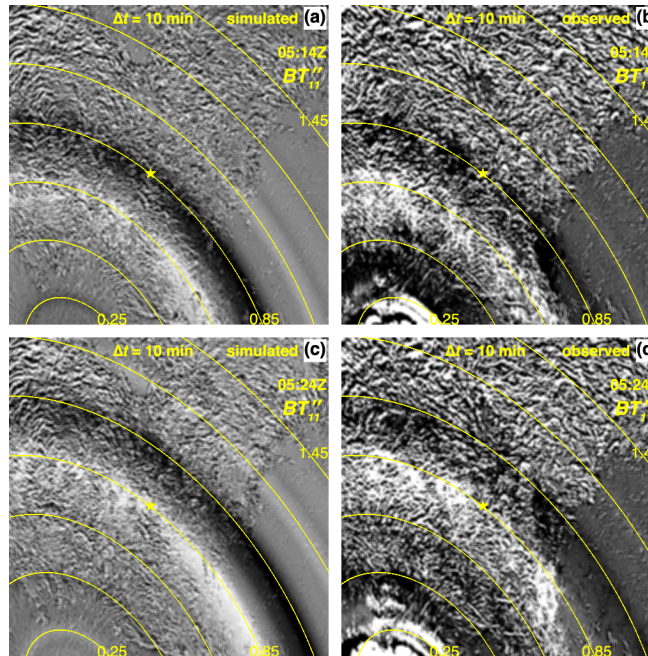
725

726

727

728

729



730 **Figure 8.** Same as Figure 7, but for  $\Delta t = 10$  min sampling.

731

### 732 3.6 Spatiotemporal aliasing

733 To summarize our results so far, the wave patterns seen in the imagery are determined by  
 734 the interplay of two opposing effects. The time derivatives amount to a high pass filter, which  
 735 highlights the shorter period fluctuations within the wave packet. Conversely, only the longer  
 736 period variations are preserved when the observation frequency is reduced. In this section, we  
 737 discuss the latter aliasing effect in more detail.

738 The minimum wavelength and wave period that can be captured in the satellite  
 739 observations are determined by the spatiotemporal characteristics of the images and basic  
 740 sampling theorem. The Nyquist–Shannon condition requires at least two samples per period  
 741 (both spatial and temporal) for successful signal reconstruction. As discussed in Section 2, the  
 742 typical grid spacing in most of the mesoscale domains is 3–6 km, depending on propagation  
 743 azimuth and location in the domain. This translates to a minimum observable horizontal  
 744 wavelength of 6–12 km. In the GOES-17 M2 Alaska domain the minimum observable  
 745 wavelength is larger, ~16–20 km, due to the reduced image resolution near the limb. The  
 746 maximum detectable wavelength, on the other hand, is equal to the domain size or ~1,000 km.

747 Similarly, the 1-min sampling period of the mesoscale scans corresponds to a minimum  
 748 resolved wave period of 2 min, or a maximum resolved frequency of 8.3 mHz. All higher  
 749 frequency variations are aliased to lower frequencies. The temporal aliasing (or under-sampling)  
 750 artifact is significantly more severe in the lower cadence full disk imagery. The shortest period  
 751 and highest frequency that can be resolved in GOES-R and Himawari-8 FD with a sampling

752 period of 10 min are 20 min and 0.83 mHz, respectively, while these cutoffs are 30 min and 0.56  
 753 mHz for Meteosat FD with a sampling period of 15 min.

754 Microbarometer measurements reported by Matoza et al. (2022) indicate that the HTHH  
 755 eruption generated infrasound ( $>10$  mHz) as well as audible sound ( $>20$  Hz), which are above  
 756 the Nyquist frequency of the mesoscale scans. Johnson et al. (2023) demonstrated that infrasonic  
 757 waves in volcanic plumes are detectable by high frame-rate video obtained in the immediate  
 758 vicinity of the vent. The amplitude of these higher-frequency waves, however, is too small to  
 759 cause noticeable perturbations in satellite observations. The satellite brightness temperatures  
 760 contain information about Lamb waves and gravity waves instead.

761 Figure 9 demonstrates the effect of longer sampling periods on the wave patterns that  
 762 emerge in the near-field  $BT''$  images. The results for the shortest sampling period of  $\Delta t = 1$  min  
 763 are compared with those for longer periods of  $\Delta t = 2, 5,$  and  $10$  min, which cover the typical  
 764 sampling rates of operational geostationary imagers: Himawari-8 rapid scan, Meteosat rapid  
 765 scan, and GOES-R and Himawari-8 full disk scan, respectively.

766 The highest temporal resolution data reveal a swarm of densely packed concentric waves  
 767 with the main pulse near the 1,200 km isodistance (Figure 9a). The waves propagate with a speed  
 768 of  $\sim 315$  m s $^{-1}$  as we show in Section 4.1. Their horizontal wavelength increases from  $\sim 40$ – $50$  km  
 769 to  $\sim 50$ – $70$  km with distance from HTHH. The increase in  $\lambda_H$  across the domain might be due to  
 770 dispersion—longer waves traveling faster—caused by vertical and horizontal variations in wind  
 771 and temperature (Garrett, 1969). Alternatively, it could be due to the emission of several  
 772 individual wave packets. There were multiple explosions between 4–6 UTC (see Figure 2a),  
 773 which could have different horizontal extent, leading to different characteristic  $\lambda_H$ .

774

775

776

777

778

779

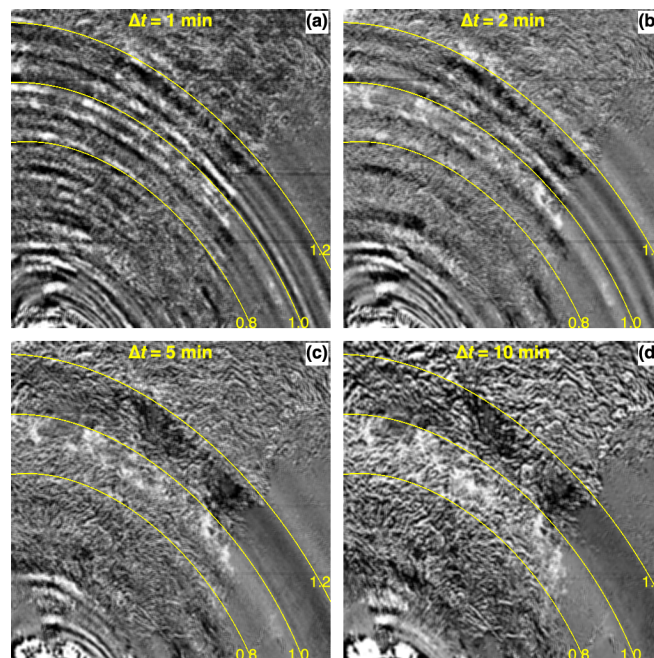
780

781

782

783

784



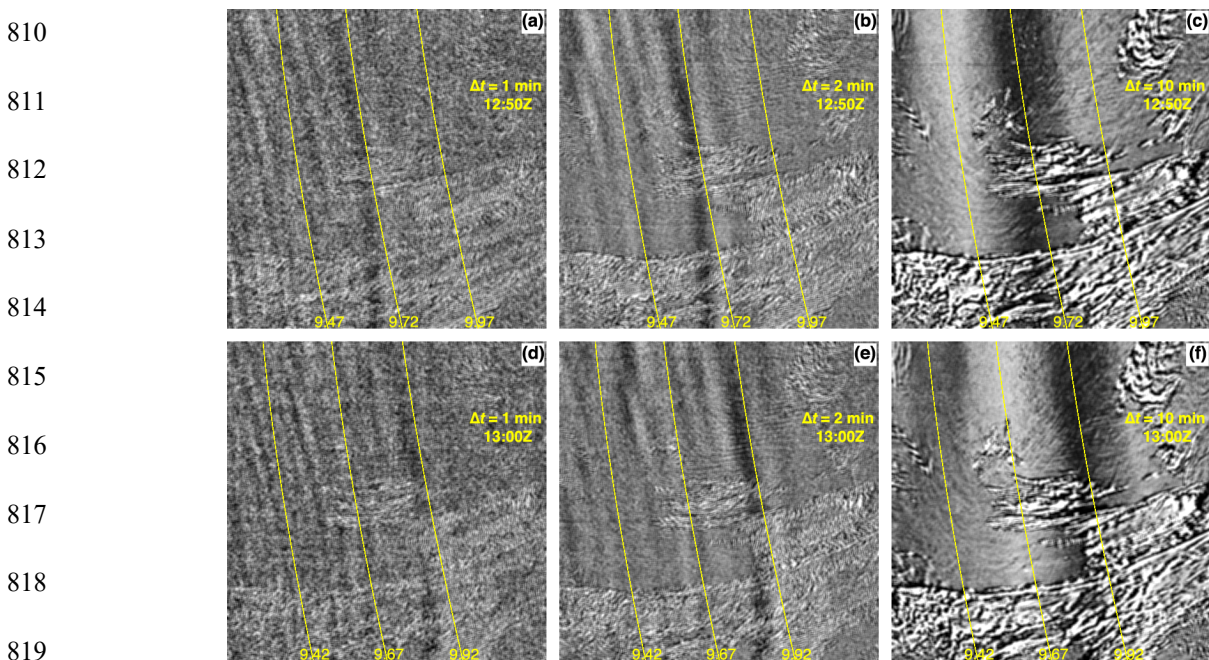
785 **Figure 9.** Near-field spatiotemporal aliasing in  $BT''_{11}$  in G17\_M2 (Samoa) at 05:30 UTC on 15  
 786 January 2022. The interval used for calculating the time derivative is (a)  $\Delta t = 1$  min, (b)  $\Delta t = 2$

787 min, (c)  $\Delta t = 5$  min, and (d)  $\Delta t = 10$  min. The images were histogram equalized and mean  
 788 filtered using a  $5 \times 5$ -pixel window. The yellow lines are isodistances ( $\times 1,000$  km) from HTHH.  
 789

790 As the sampling period gets longer, the fine detail in the  $BT$  time derivatives is gradually  
 791 lost (Figures 9b-9c-9d). This is the manifestation of spatiotemporal aliasing, where frequencies  
 792 above the Nyquist frequency of the given sampling rate become aliased to lower frequencies and  
 793 longer wavelengths, resulting in an effect resembling ‘motion blur’. Some loss of detail is  
 794 already noticeable for  $\Delta t = 2$  min, but for full disk sampling with  $\Delta t = 10$  min, the observed  
 795 pattern is reduced to  $\sim 200$  km wide dark and bright bands as shown previously in Figure 8.

796 The aliasing in a far-field domain is depicted in Figure 10. At high frequency sampling  
 797 ( $\Delta t = 1$  or 2 min), the main Lamb pulse is represented by the dark band near the 9,720 km  
 798 isodistance in the 12:50 UTC image. There is a fainter dark band  $\sim 120$ – $140$  km ahead (east) of  
 799 the main pulse, which corresponds to the smaller pressure peak emitted  $\sim 7$  min earlier (see  
 800 Figures 2a and S1). Here we note that Vadas et al. (2023b) analyzed  $4.3\text{-}\mu\text{m}$   $BT$  perturbations in  
 801 an Atmospheric Infrared Sounder (AIRS) granule over Antarctica ( $7,500$ – $8,000$  km from  
 802 HTHH). They found a Lamb amplitude peak at a wavelength of  $\sim 146$  km, which agrees with our  
 803 finding for the distance between the main pressure peak and the preceding one.

804 The main pulse is followed by a long train of waves with wavelengths decreasing in time  
 805 from  $\sim 65$ – $75$  km to  $\sim 40$ – $50$  km, which again suggests dispersion. Full disk sampling ( $\Delta t = 10$   
 806 min) only reveals the primary pulse, with the dark and bright bands having an increased width  
 807 and wavelength of  $\sim 250$  km and  $\sim 500$  km, respectively, compared to the near field. The waves  
 808 travel with a slightly larger observed propagation velocity of  $\sim 330$  m  $\text{s}^{-1}$ , which likely is due to  
 809 the added effect of westerly winds in this domain.



820 **Figure 10.** Far-field spatiotemporal aliasing in  $BT''_{12}$  in G16\_M2 (Texas) at **(top row)** 12:50  
 821 UTC and **(bottom row)** 13:00 UTC on 15 January 2022. The interval used for calculating the

822 time derivative is **(a, d)**  $\Delta t = 1$  min, **(b, e)**  $\Delta t = 2$  min, and **(c, f)**  $\Delta t = 10$  min. The images were  
 823 histogram equalized and mean filtered using a  $5 \times 5$ -pixel window. The yellow lines are  
 824 isodistances ( $\times 1000$  km) from HTHH.

## 825 **4 Far-field Lamb waves and near-field gravity waves**

### 826 4.1 Minor arc and major arc passage of Lamb waves

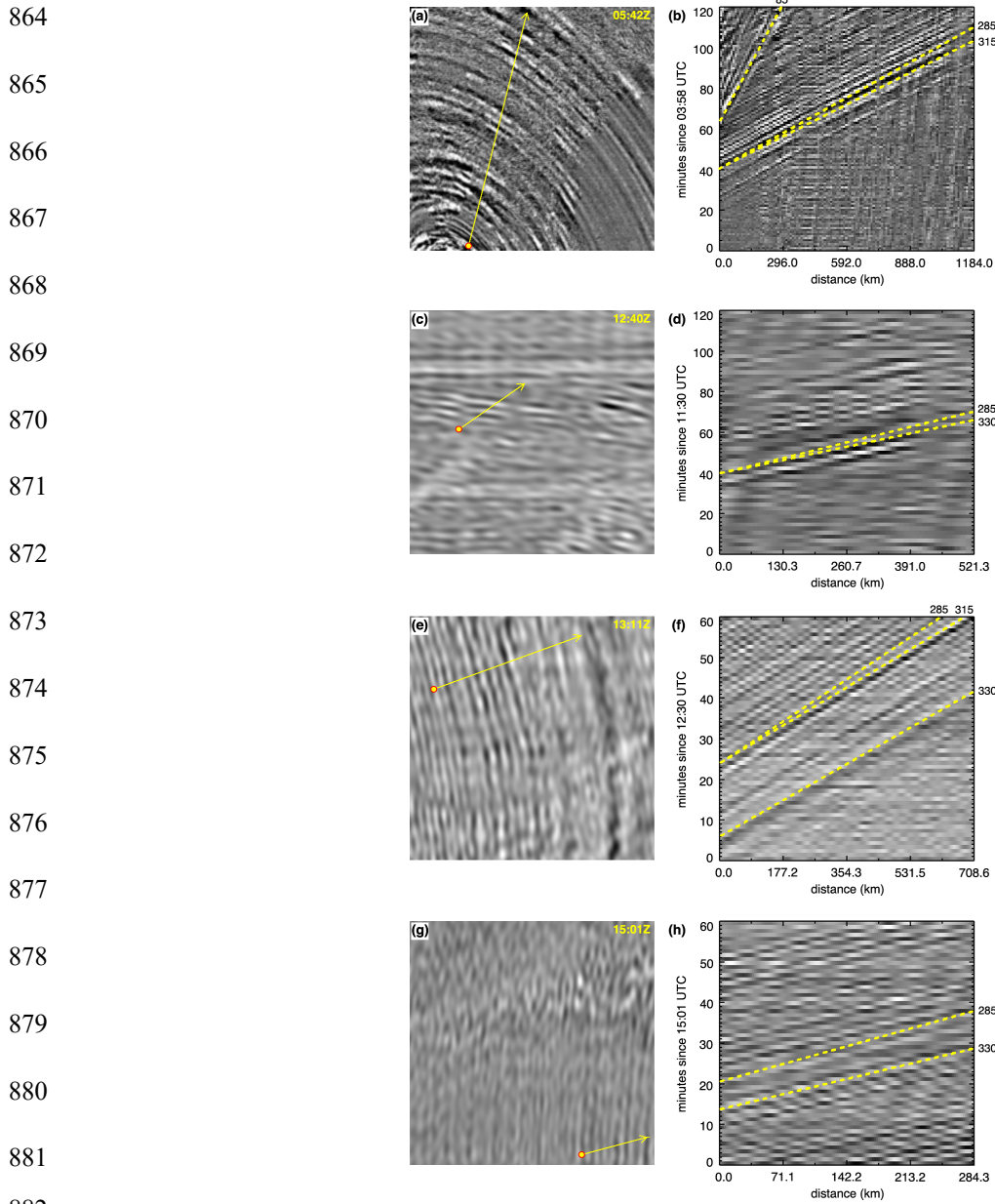
827 In this section, we track the first minor arc (A1, from west to east towards the antipode)  
 828 and major arc (A2, from east to west towards HTHH) passage of the waves across the mesoscale  
 829 domains on 15 and 16 January 2022, respectively. The third and fourth passages are also weakly  
 830 detectable in the data, but we focus on the stronger and more informative signature of the first  
 831 two passages. The ground-based propagation speed of the waves is estimated with the help of  
 832 time–distance plots introduced in Figure 11. A time–distance plot is constructed by stacking 1D  
 833 slices of the  $BT''$  images taken along a path marked by the yellow arrow. The path is aligned  
 834 with a fixed back-azimuth and indicates the overall propagation direction. In such a stack plot,  
 835 wave crests and troughs traveling along the path are represented by bright and dark stripes,  
 836 whose slope encodes the propagation speed. With distance on the x-axis and time on the y-axis,  
 837 the slope decreases with increasing speed.

838 For simplicity, we use line segments as paths, which, nevertheless, are well aligned with  
 839 geodesics over the mesoscale distances considered here. Due to the spatial (pixel) discretization,  
 840 the speed estimates are virtually insensitive to a  $5^\circ$ – $10^\circ$  variation in the back-azimuth of the  
 841 segment.

842 The longer the line segment, however, the better the separation of stripes corresponding  
 843 to different speeds. The longest possible segment is the domain's diagonal, which is  $\sim 2,000$  km  
 844 for the near-field and  $\sim 1,500$  km for the far-field domains. In practice, however, the length of the  
 845 line segment available for tracking is significantly shorter, because the waves are visible only in  
 846 certain parts of the domain. In our case, the length of segments used for speed estimation ranges  
 847 between  $\sim 300$ – $1,200$  km. Over such distances, the travel time difference between speeds of  $285$   
 848  $\text{m s}^{-1}$  and  $315 \text{ m s}^{-1}$  varies from 1.7 min to 6.7 min. These travel time differences correspond to a  
 849 mere 2–6 or 1–3 tick mark separation along the y-axis for  $\Delta t = 1$  min and  $\Delta t = 2$  min sampling,  
 850 respectively. Thus, a variation of  $30 \text{ m s}^{-1}$  (or 10%) around the sound speed is slightly or just  
 851 barely distinguishable in the mesoscale data, depending on the length of the segment and the  
 852 sampling period. This uncertainty should be kept in mind when interpreting the stack plots.

853 The initial passage of A1 waves across the GOES-17 M2 Samoa domain between 04:00–  
 854 06:00 UTC on 15 January is shown in Movie S3 and Figures 11a-b. The first visually detectable  
 855 wave appears at the bottom of the domain  $\sim 170$  km from HTHH at 04:16 UTC. The time–  
 856 distance plot reveals the passage of more than a dozen wave crests during this 2-hour period. The  
 857 observed speed clearly exceeds the GW speed limit of  $\sim 285 \text{ m s}^{-1}$  (see Extended Data Figure 6 in  
 858 Wright et al., 2022) and is estimated at  $\sim 315 \text{ m s}^{-1}$ . This velocity combined with the arrival time  
 859 puts the emission time of the first wave at  $\sim 04:07$  UTC, which agrees with the time of the first  
 860 eruptive event in the Samoa surface pressure (Figure 2a) as well as in distant infrasound and  
 861 seismo-acoustic records (Matoza et al., 2022). The wave fronts follow isodistances very well,  
 862 indicating isotropic propagation in the near field.

863



883 **Figure 11.** Passage of A1 waves across the mesoscale domains on 15 January 2022. From top to  
 884 bottom: **(a, b)** G17\_M2 (Samoa) 03:58–05:58 UTC, C11, **(c, d)** G17\_M2 (Alaska) 11:30–13:30  
 885 UTC, C11, **(e, f)** G16\_M2 (Texas) 12:30–13:30 UTC, C12, and **(g, h)** G16\_M1 (Alabama)  
 886 15:01–16:01 UTC, C09 (6.9  $\mu\text{m}$ ). The left panels are snapshots of  $BT''$  at the indicated times and  
 887 the right panels are time–distance plots over 1- or 2-hour periods with guides of constant phase  
 888 speed drawn (dashed yellow, in  $\text{m s}^{-1}$ ). The yellow arrows are aligned with fixed back-azimuths  
 889 and indicate the overall propagation direction. Distance is measured from the circle (0 km)  
 890 towards the arrowhead. The interval used for calculating  $BT''$  is  $\Delta t = 2$  min for G17\_M2  
 891 (Alaska) and  $\Delta t = 1$  min otherwise. Except for the top row, the  $BT''$  images were FFT-filtered.

892

893 The horizontal wavelength tends to increase from  $\sim 40$  km to  $\sim 70$  km with increasing  
894 distance from HTHH (period 2.1–3.7 min, frequency 4.5–7.9 mHz), suggesting some dispersion.  
895 The corresponding relatively small variations in speed, however, cannot be clearly detected  
896 given the uncertainty of our estimation method. The steeper stripes in the top-left corner of the  
897 stack plot represent slower GWs traveling with a speed of  $\leq 85$  m s<sup>-1</sup>, which appear in the  
898 stratospheric umbrella cloud as it intrudes into the domain after  $\sim 05:00$  UTC.

899 Tracking the waves in the near-limb GOES-17 M2 Alaska domain is more difficult due to  
900 the coarse pixel size and considerable horizontal striping. To increase the signal to noise ratio  
901 (SNR), we used  $\Delta t = 2$  min sampling and applied FFT filtering to the images when constructing  
902 the stack plot (Movie S4 and Figures 6c-d). The waves are first visible near the bottom left  
903 (southwest) corner of the domain at  $\sim 11:15$  UTC. Waves with longer  $\lambda_H \approx 90$ –110 km enter  
904 first, followed by waves with somewhat shorter  $\lambda_H \approx 70$ –90 km. The wavelength of subsequent  
905 waves cannot be estimated with confidence. Here, a propagation speed of  $\sim 330$  m s<sup>-1</sup> is a  
906 marginally better fit than the previously estimated  $\sim 315$  m s<sup>-1</sup>, at least for the longer wavelength  
907 waves that produce the clearest signal. Note that audible sound was reported at Kenai, Alaska  
908 between 13:15–13:45 UTC (Matoza et al., 2022), which is at the end of the 2-hour period when  
909 the passage of the wave train was detectable in the mesoscale data.

910 As the waves travel eastward, they enter the GOES-16 M2 (Texas) domain at  $\sim 12:20$   
911 UTC (Movie S5 and Figures 11e-f). The main Lamb pulse is detected first, followed by waves  
912 with a  $\lambda_H$  that generally decreases in time from  $\sim 75$  km to  $\sim 40$  km (frequency 4.2–7.9 mHz).  
913 Waves can be observed in this domain at least until 15:00 UTC. Here, wave dispersion is perhaps  
914 also borne out by the stack plot speed estimates. The main pulse appears to propagate at a speed  
915 of  $\sim 330$  m s<sup>-1</sup>, while the traces of later wave fronts are better explained by a reduced speed of  
916  $\sim 315$  m s<sup>-1</sup>. These waves are likely Lamb waves, because they travel faster than the absolute  
917 maximum GW speed limit of  $\sim 285$  m s<sup>-1</sup>, which is too slow to fit the data.

918 Finally, the waves are observed in the bottom half of our easternmost GOES-16 M1  
919 (Alabama) domain between 15:01–16:20 UTC (Movie S6 and Figures 11g-h). This domain  
920 misses the main pulse and only captures the subsequent shorter waves with  $\lambda_H \approx 40$ –55 km.  
921 Because the waves can be best tracked over a short line segment in the bottom right corner,  
922 speed estimation from the stack plot is relatively uncertain. The wave traces indicate a  
923 propagation speed between 315–330 m s<sup>-1</sup>.

924 By the time the waves reach the continental US, the wave fronts exhibit small but  
925 noticeable deviations from the isodistances. As shown in Figure 12 for the GOES-16 M2 Texas  
926 domain, the wave fronts travel faster in the middle than at the top or bottom of the domain (see  
927 also Figures 10 and 11e). The maximum deviation is  $\sim 120$  km for the main Lamb pulse and  $\sim 50$   
928 km for the shorter-wavelength trailing waves. If we assume that the main pulse was emitted at  
929  $\sim 04:29$  UTC, the acquisition time and distance from HTHH lead to a mean propagation speed in  
930 the middle and at the bottom of the domain of  $\sim 323$  m s<sup>-1</sup> and  $\sim 319$  m s<sup>-1</sup>, respectively—in good  
931 agreement with the stack plot estimate of  $\sim 315$  m s<sup>-1</sup>. This  $\sim 4$  m s<sup>-1</sup> mean speed difference  
932 amounts to a remarkably small,  $\sim 1.3\%$  anisotropy in propagation along paths that go over the  
933 US. In full-disk data, Wright et al. (2022) found larger deviations from isodistances in the  
934 portion of the main pulse which passed over the northern half of South America and slowed. The  
935 observed propagation anisotropy can likely be explained by temperature and wind variations as  
936 well as topography effects encountered along the travel path as argued by Sepúlveda et al. (2023)  
937 and Watada et al. (2023).

938

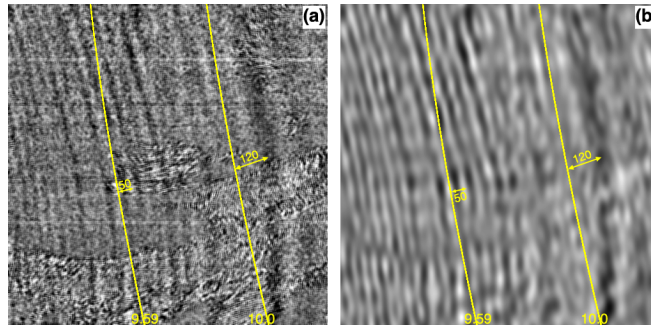
939

940

941

942

943



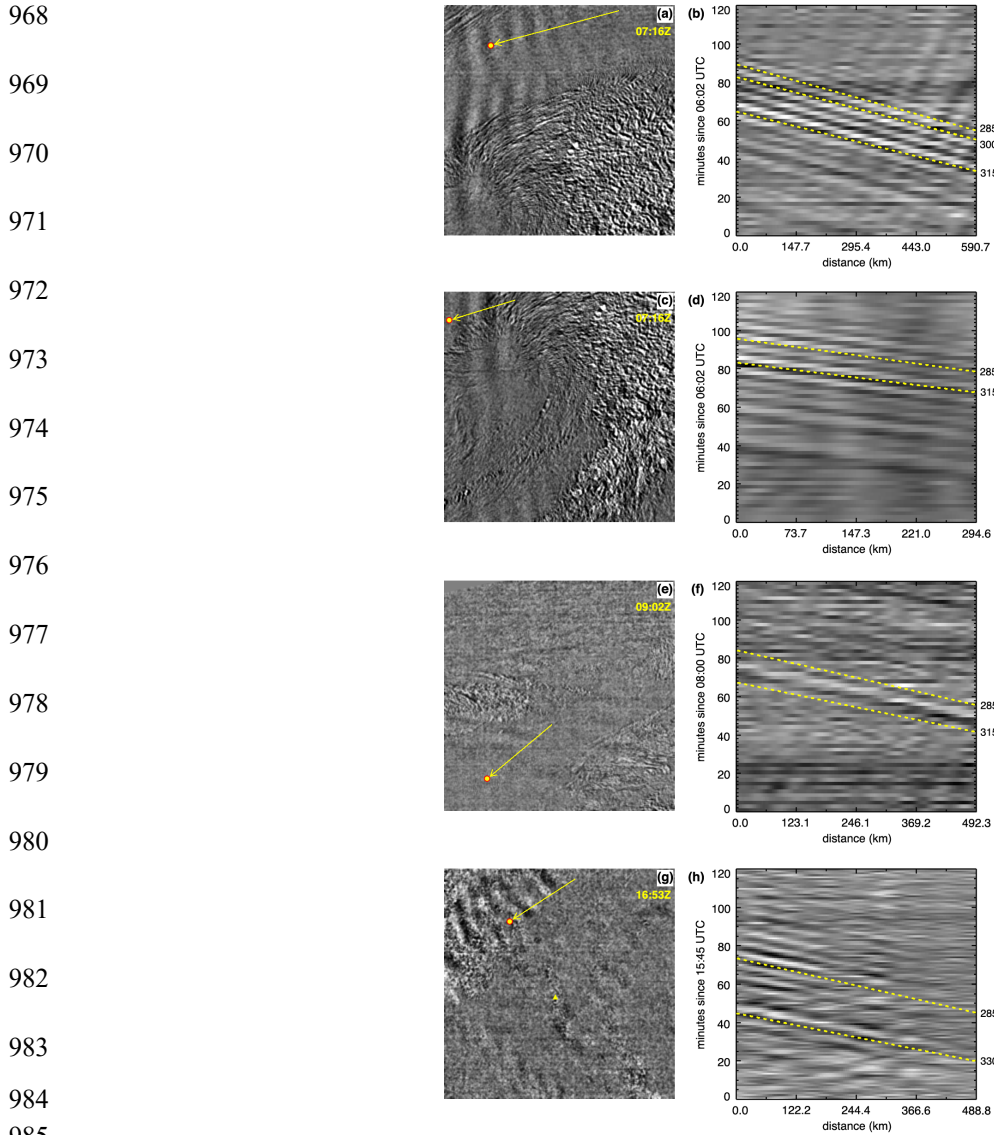
944 **Figure 12.** Anisotropic wave propagation in G16\_M2 (Texas): **(a)** raw grayscale image and **(b)**  
 945 FFT-filtered image of  $BT''_{12}$  at 13:11 UTC on 15 January 2022. The interval used for calculating  
 946 the time derivative is  $\Delta t = 1$  min. The yellow lines are isodistances ( $\times 1,000$  km) from HTHH,  
 947 which were fitted to the bottom (southernmost) part of the thickest dark band (at 10k km) and  
 948 one of the thinner white bands (at 9.59k km). The width of the dark band is  $\sim 50$  km, while that of  
 949 the white band is  $\sim 25$  km. The maximum deviation of the midline of the wave bands from the  
 950 fitted isodistances is also indicated ( $\sim 120$  km and  $\sim 50$  km, respectively).

951

952 The A2 antipodal passage of the waves is shown in Figure 13 and Movies S7–S10.  
 953 Because the signal becomes weaker during the longer major arc paths, we used  $\Delta t = 2$  min  
 954 sampling to increase the SNR. As before, the observed wavelength tends to decrease in time,  
 955 suggesting wave dispersion. However, the visually detectable wavelengths shift towards larger  
 956 values compared to the A1 passage and are typically within 95–120 km. The disappearance of  
 957 shorter wavelengths is likely caused by the increased (acoustic) attenuation at higher frequencies.

958 The estimated propagation speed is in the range of  $300\text{--}330$  m  $s^{-1}$ . In the US domains,  
 959 there is a hint of a slightly faster A1 passage (maximum  $\sim 330$  m  $s^{-1}$ ) than A2 passage (maximum  
 960  $\sim 315$  m  $s^{-1}$ ), which likely is due to the waves traveling with the midlatitude westerlies in the  
 961 former case but traveling against them in the latter case. This observed speed reduction agrees  
 962 with the modeling by Sepúlveda et al. (2023), which accounts for wind effects: the apparent  
 963 phase speed decreases when the Lamb wave propagates against the wind and vice versa. Also  
 964 note the complex interference patterns as the returning waves enter from different azimuths at  
 965 different times and converge in the HTHH domain after circling the planet (Movie S10). Such  
 966 complex far-field waveforms are produced and shaped by global wind variations.

967



986 **Figure 13.** Passage of A2 waves across the mesoscale domains on 16 January 2022. From top to  
 987 bottom: **(a, b)** G16\_M2 (Indiana) 06:02–08:02 UTC, C09, **(c, d)** G16\_M1 (Alabama) 06:02–  
 988 08:02 UTC, C09, **(e, f)** G17\_M2 (Alaska) 08:00–10:00 UTC, C11, and **(g, h)** G17\_M1 (HTHH)  
 989 15:45–17:45 UTC, C07. The left panels are snapshots of  $BT''$  at the indicated times and the right  
 990 panels are time–distance plots over 2-hour periods with guides of constant phase speed drawn  
 991 (dashed yellow, in  $\text{m s}^{-1}$ ). The yellow arrows are aligned with fixed back-azimuths and indicate  
 992 the overall propagation direction. Distance is measured from the circle (0 km) towards the base  
 993 of the arrow. The interval used for calculating  $BT''$  is  $\Delta t = 1$  min for G17\_M1 (HTHH) and  
 994  $\Delta t = 2$  min otherwise. The snapshots in the left column are unfiltered images, while the time–  
 995 distance plots in the right column are based on low pass-filtered images. The yellow triangle in  
 996 panel **(g)** marks the location of HTHH.

997

## 998 4.2 Wave phenomena observed over the plume

999           So far, we have focused on far-field domains which did not observe the plume itself. The  
 1000 GOES-17 M1 domain, however, was moved to HTHH ~3 hours after the main eruption at 07:05  
 1001 UTC on 15 January and remained there for 2 days. This domain allows us to study the generation  
 1002 and propagation of waves directly over the plume. Below we present three examples that  
 1003 demonstrate the potential of this data source. We focus on the first two hours of the data, because  
 1004 later imagery shows increased noise and striping, although waves are detectable at least until  
 1005 14:00 UTC.

### 1006 4.2.1 GWs obscured by the stratospheric umbrella

1007           A case when GWs are observed in the tropospheric umbrella but not in the stratospheric  
 1008 umbrella was captured during the first hour of the GOES-17 M1 HTHH data between 07:06–  
 1009 08:06 UTC (Movie S11). At that time the plume consists of two distinct layers, as shown by the  
 1010 10.3  $\mu\text{m}$  (band 13, ‘clean’ longwave window) brightness temperatures in Figure 14a. The  
 1011 warmer stratospheric umbrella (~230K, light gray) is located between 30–35 km, while the  
 1012 colder near-tropopause umbrella (~195K, white) is spreading between 16–19 km. The eastward-  
 1013 propagating concentric arcs of short-wavelength GWs are clearly visible in the near-tropopause  
 1014 umbrella; however, their westward-propagating counterparts are absent from the stratospheric  
 1015 umbrella, as depicted by the  $BT''_{13}$  images in Figure 14b. The stack plot in Figure 14c indicates  
 1016 horizontal wavelengths of ~13–18 km and phase speeds of ~45–50  $\text{m s}^{-1}$  (periods of ~4.8–6.0  
 1017 min and frequencies of ~2.8–3.5 mHz). Note that at full-disk sampling ( $\Delta t = 10$  min), these  
 1018 eastward-propagating short GWs seemingly move westward due to the wagon-wheel temporal  
 1019 aliasing effect (Movie S12).

1020           If the source of these waves is below the tropopause, a potential explanation is critical  
 1021 level filtering. When the horizontal phase speed of upward propagating gravity waves equals the  
 1022 projection of the background wind speed along the GW propagation direction at a given altitude,  
 1023 the vertical component of group velocity approaches zero. At that critical level, the GWs are  
 1024 eliminated as their energy is absorbed and transferred to the background flow. This leads to the  
 1025 blocking of wave propagation in certain directions, depending on the wind profile.

1026           A reanalysis mean wind profile is available from ERA5 (Hersbach et al., 2017;  
 1027 Supporting Information Figure S4), while actual plume motion and height retrievals were  
 1028 obtained by Carr et al. (2022) using stereo observations from Himawari-8 FD and GOES-17 M1  
 1029 HTHH imagery. Both wind datasets show weak meridional winds typically between  $\pm 5$   $\text{m s}^{-1}$   
 1030 throughout the entire troposphere and stratosphere. The zonal winds were eastwardly and  
 1031 relatively weak in the troposphere and near the tropopause; for the 16–19 km altitude range  
 1032 varying between 0–10  $\text{m s}^{-1}$  in ERA5 and between 0–15  $\text{m s}^{-1}$  with a mean of ~7  $\text{m s}^{-1}$  in the  
 1033 stereo retrievals. Such weak winds have little effect on the eastward-propagating GWs detected  
 1034 in the lower umbrella.

1035

1036

1037

1038

1039

1040

1041

1042

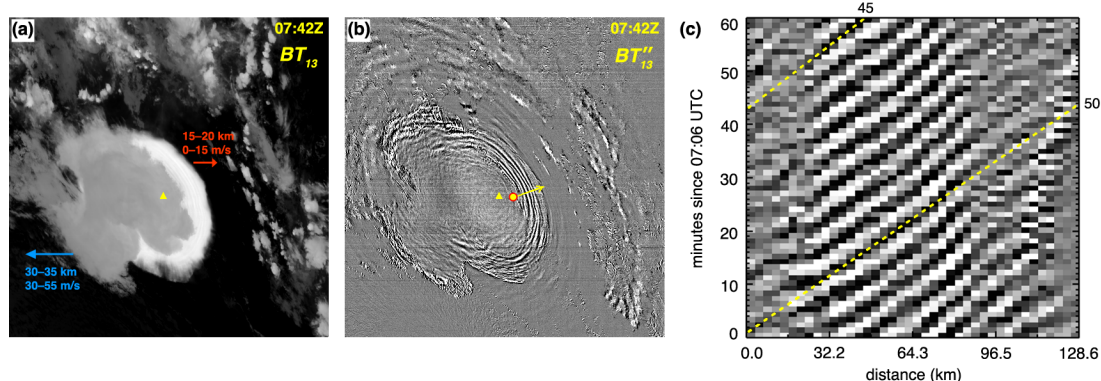
1043

1044

1045

1046

1047



1048 **Figure 14.** GW obscuration in G17\_M1 (HTHH) on 15 January 2022: **(a)** channel 13 ( $10.3\ \mu\text{m}$ )  
 1049 brightness temperatures  $BT_{13}$  at 07:42 UTC, **(b)**  $BT''_{13}$  at 07:42 UTC, and **(c)** time–distance plot  
 1050 for the period 07:06–08:06 UTC along the yellow arrow in panel **(b)**. The interval used for  
 1051 calculating the time derivatives is  $\Delta t = 1\ \text{min}$ .  $BT_{13}$  was gray scaled between 190K (white) and  
 1052 290K (black), but no filtering was applied to  $BT''_{13}$ . The yellow triangle marks the location of  
 1053 HTHH. The height range and typical zonal velocity of the stratospheric and near-tropopause  
 1054 plumes are also indicated in panel **(a)**.

1055

1056 In the mid stratosphere, however, the zonal winds were westwardly and much faster. In  
 1057 the 30–35 km altitude range of the upper umbrella, ERA5 indicates westward winds of 25–35 m  
 1058  $\text{s}^{-1}$ . The stereo wind retrievals are significantly stronger, showing westward plume motion of 30–  
 1059 55  $\text{m s}^{-1}$ . Thus, stratospheric plume motion is fast enough for critical level filtering to eliminate  
 1060 westward-propagating GWs emitted below the tropopause.

1061 AIRS observations, however, show similar waves to the west of the volcano a few hours  
 1062 later (Wright et al., 2022). If the GWs are emitted in a region extending from the tropopause to  
 1063 the lower stratosphere, critical level filtering is unlikely to play a major role. The GWs might  
 1064 simply be obscured by the optically thick mid-stratospheric plume, which masks the  $BT$   
 1065 perturbations.

#### 1066 4.2.2 Mean flow advection of GWs

1067 Strong winds can horizontally shift the apparent center of concentric gravity waves,  
 1068 which was clearly demonstrated by the modeling study of Vadas et al. (2009). This effect is also  
 1069 observed in the first hour of the GOES-17 M1 HTHH data stream. Here we focus on faster GWs  
 1070 that are already noticeable in the northwestern (top left) corner of Figure 14b. These GWs,  
 1071 however, can be detected more clearly in the 9.6- $\mu\text{m}$  ‘ozone’ channel (C12), especially after  
 1072 FFT-filtering, as shown in Figure 15a (see also Movie S13). The vertical weighting function of  
 1073 C12 peaks at  $\sim 22\ \text{km}$ , thus, the GWs are captured at a higher altitude, near the mid stratosphere,  
 1074 compared to the 10.3- $\mu\text{m}$  window channel. The stack plot in Figure 15b indicates horizontal  
 1075 wavelengths of  $\sim 32\text{--}42\ \text{km}$  and phase speeds of  $\sim 130\text{--}135\ \text{m s}^{-1}$  (typical period of  $\sim 4.7\ \text{min}$  and  
 1076 frequency of  $\sim 3.5\ \text{mHz}$ ). Note that this speed is essentially the theoretical maximum GW phase  
 1077 speed at this particular wavelength (see Extended Data Figure 6 in Wright et al., 2022).

1078 It is evident in Figure 15a that the concentric rings cannot be fitted with ellipses centered

1079 on HTHH. A caveat to note is that the emission center of GWs in the satellite images is always  
 1080 shifted from HTHH, even in windless conditions, due to parallax. Because GOES-17 views  
 1081 HTHH from the east-northeast (azimuth of  $66^\circ$ ) at a zenith angle of  $50^\circ$ , the apparent emission  
 1082 center is shifted to west-southwest (left and below) relative to HTHH by a distance depending on  
 1083 the emission height. For an emission height of 17 km (lower umbrella) and 32 km (upper  
 1084 umbrella) the shift is  $\sim 20$  km and  $\sim 38$  km, respectively, or  $\mathcal{O}(10)$  pixels).

1085

1086

1087

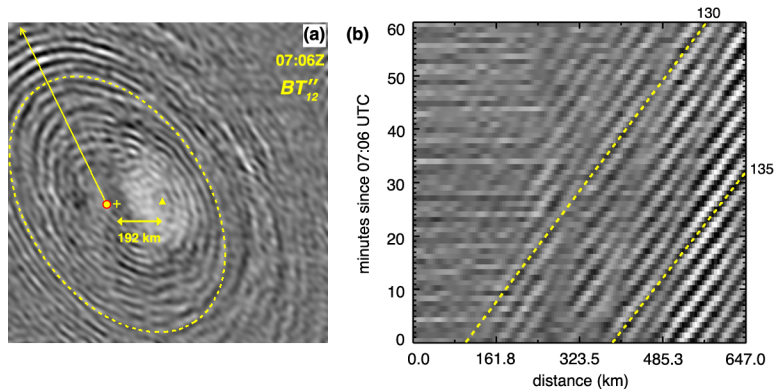
1088

1089

1090

1091

1092



1093 **Figure 15.** Mean flow advection in G17\_M1 (HTHH) on 15 January 2022: **(a)** FFT-filtered  $BT''_{12}$   
 1094 at 07:06 UTC and **(b)** time–distance plot for the period 07:06–08:06 UTC along the yellow  
 1095 arrow in panel **(a)**. The interval used for calculating the time derivatives is  $\Delta t = 1$  min. The  
 1096 yellow dashed curve is an ellipse fitted to one of the concentric rings with its center marked by  
 1097 the plus sign. The distance between the ellipse center and HTHH (yellow triangle) is also  
 1098 indicated.

1099

1100 The center of the ellipse fitted to one of the concentric rings in Figure 15a is located  $\sim 192$   
 1101 km west of an assumed emission source at  $\sim 22$  km (peak of C12 weighting function). Note that  
 1102 the uncertainty of ellipse fitting can easily be on the order of 10 km, because the concentric rings  
 1103 are not perfect circles (or ellipses in the satellite perspective) due to anisotropic propagation and  
 1104 they might only be partially observed. Here we focused on fitting the northern and western part  
 1105 of the rings, which are the clearest in the images.

1106 The semi major axis of the fitted ellipse is  $\sim 461$  km, which corresponds to a travel time  
 1107 of  $\sim 59$  min from emission assuming a propagation velocity of  $130 \text{ m s}^{-1}$ . This, in turn,  
 1108 corresponds to a mean westward advection speed of the ellipse center of  $\sim 54 \text{ m s}^{-1}$ . By fitting  
 1109 several concentric rings, we estimate a typical westward advection speed of  $50\text{--}60 \text{ m s}^{-1}$ , which  
 1110 is within the range of the stereo plume motion retrievals by Carr et al. (2022). The largest ring in  
 1111 Figure 15a indicates a travel time of  $\sim 75$  min; therefore, these GWs were likely triggered by a  
 1112 later explosion which started between 05:44–05:51 UTC according to surface pressure records  
 1113 (Purkis et al., 2023; Wright et al., 2022).

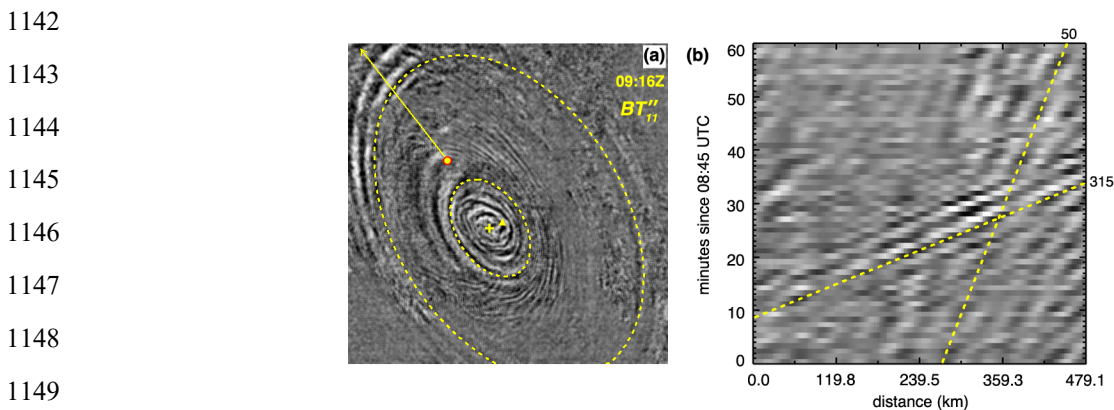
#### 1114 4.2.3 Lamb waves from the last major explosion

1115 Our final example using the GOES-17 M1 HTHH imagery demonstrates the detection of  
 1116 Lamb waves triggered by the last major eruption  $\sim 4.0\text{--}4.5$  hours after the primary climactic  
 1117 event. The  $10.3\text{-}\mu\text{m}$  brightness temperatures show several cold bubbles rising to 30+ km altitude

1118 between 8–9 UTC (Movie S11; Carr et al., 2022), with the two most prominent ones occurring at  
 1119 08:41 UTC (~168K) and 08:46 UTC (~172K). Stereo motion retrievals by Carr et al. (2022)  
 1120 reveal strong plume-top divergence as these bubbles reach the upper umbrella and spread out.  
 1121 The global infrasound and seismo-acoustic network detected an explosive event at 08:31 UTC  
 1122 (Matoza et al., 2022), while the Tonga surface pressure data indicate the last major signal at  
 1123 08:46 UTC (Wright et al., 2022).

1124 This series of explosions generated Lamb waves as well as GWs, as depicted in Figure 16  
 1125 (see also Movie S14). The animations show a fast-moving packet of waves in the top left  
 1126 (northwestern) quadrant of the domain between ~08:55–09:30 UTC. The stack plot in Figure 16b  
 1127 yields a propagation speed of  $\sim 315 \text{ m s}^{-1}$  and horizontal wavelength of  $\sim 60\text{--}70 \text{ km}$ , similar to the  
 1128 Lamb waves generated by the primary explosion. Unlike the primary Lamb waves, however  
 1129 these weaker secondary Lamb waves could not be detected in the far-field domains. Note that the  
 1130 concentric rings in Figure 16a can be well fitted with circles centered on HTHH. This indicates  
 1131 negligible parallax in the projected location of the emission center, which is further proof of  
 1132 surface-triggered Lamb waves that coherently move through the troposphere guided by weak  
 1133 near-surface winds.

1134 In contrast, the smaller concentric rings visible in the upper umbrella can only be fitted  
 1135 with circles whose center is shifted west-southwest relative to HTHH due mostly to parallax and  
 1136 to a lesser degree wind. This indicates gravity waves emitted at 30+ km altitude. A time–distance  
 1137 analysis (not shown) reveals that the spectral characteristics of these GWs (wavelength of  $\sim 40$   
 1138 km and speed of  $\sim 135 \text{ m s}^{-1}$ ) are similar to those of the earlier-emitted GWs plotted in Figure 15.  
 1139 Figure 16b also hints at the presence of slower GWs propagating at a speed of  $\sim 40\text{--}50 \text{ m s}^{-1}$ .  
 1140 These small-scale GWs detected in the plume are consistent with the dense concentric wave  
 1141 patterns observed by AIRS at a somewhat larger distance from the volcano (Adam, 2022).



1150 **Figure 16.** Lamb and gravity waves in G17\_M1 (HTHH) triggered by the last major explosion  
 1151 on 15 January 2022: **(a)**  $BT''_{11}$  at 09:16 UTC and **(b)** time–distance plot for the period 08:45–  
 1152 09:45 UTC along the yellow arrow in panel **(a)**. The interval used for calculating the time  
 1153 derivatives is  $\Delta t = 1 \text{ min}$  and the stack plot is based on FFT-filtered images. The larger ellipse  
 1154 fitted to a Lamb wave ring is a circle with a radius of 585 km centered on HTHH (triangle),  
 1155 while the smaller ellipse fitted to a GW ring is a circle of 175 km radius with a shifted center  
 1156 (plus sign).

1157

1158 **5 Discussion and Summary**

1159 We analyzed GOES-R high-cadence mesoscale imagery to estimate the spectral  
1160 properties of Lamb and gravity waves emitted by the 15 January 2022 HTHH eruption. In a  
1161  $\sim 1,000 \times 1,000$  km<sup>2</sup> domain, the 1-min mesoscale brightness temperatures provide an order of  
1162 magnitude better temporal sampling than the 10-min or 15-min full-disk data used in previous  
1163 studies. The absolute temperature perturbations produced by the eruption are generally difficult  
1164 to extract, because they are superimposed on a large dynamic range and highly variable  
1165 background. Instead, we used the common visualization method of differencing  $BT$  image  
1166 sequences, which amounts to taking the time derivatives of the waveform. The appearance of  
1167 wave patterns in such difference imagery is controlled by two opposing factors. Waveform  
1168 derivatives represent a high-pass filter, which eliminates the long period variation. Contrarily,  
1169 reducing the observation frequency, as in full-disk data, leads to the temporal aliasing of short-  
1170 period fluctuations to longer periods and wavelengths.

1171 The surface pressure signature of the HTHH Lamb waves contains multiple pulses of  
1172 varying magnitude, but its broad envelope can be approximated by an  $N$ -wave or positive  
1173 triangular pulse of 20–50 min duration and 400–900 km width, depending on location. We  
1174 showed that imposing temperature anomalies that trace the measured surface pressure anomalies  
1175 explains the salient features of the  $BT''$  second derivative patterns seen in the high-cadence  
1176 mesoscale imagery. These patterns visualize the short-period variations and individual shocks  
1177 within the wave packet rather than the broad envelope. However, the full temperature anomaly  
1178 waveform can be reconstructed reasonably well from the observed mesoscale  $BT''$ . The  
1179 reconstructed temperature anomalies highly correlate with the measured pressure anomalies.

1180 In contrast, the temporally aliased full-disk data only captures the primary Lamb pulse,  
1181 which can be approximated by an  $N$ -wave with a duration of 30–40 min. In the low-cadence full-  
1182 disk  $BT''$  images, the primary Lamb pulse appears as a bright–dark–bright triplet of  $\sim 200$  km  
1183 wide bands (the distance an acoustic packet travels in 10 min).

1184 The mesoscale imagery indicates that the primary Lamb wave is trailed by long-  
1185 continuing waves of  $\sim 40$ – $80$  km wavelength. With the estimated horizontal phase velocity of  
1186  $\sim 315 \pm 15$  m s<sup>-1</sup>, the trailing waves have typical periods of 2.1–4.2 min and frequencies of 4–8  
1187 mHz. The mesoscale data also suggest dispersion, because wavelength tends to systematically  
1188 decrease with time as the wave train traverses the domains.

1189 These transient volcanic Lamb frequencies are well within the 0.2–10 mHz frequency  
1190 range of turbulence-induced background Lamb waves, which are generally present in the  
1191 atmosphere (Nishida et al., 2014). The short acoustic periods observed in our data are also in  
1192 agreement with early findings on atmospheric nuclear explosions and other major volcanic  
1193 eruptions. We note that most of the early works analyzed data from microbarovariographs, which  
1194 are high-pass instruments. They measure the rate of change of pressure (the first time derivative)  
1195 rather than the absolute pressure; thus, they are readily comparable with our observations of  $BT$   
1196 waveform derivatives.

1197 The oscillatory part of microbarovariograms recorded after nuclear tests contains  
1198 dominant wavelengths less than 100 km and periods of 1–10 min (Donn & Ewing, 1962; Donn et  
1199 al., 1963; Garrett, 1969; Pierce & Posey, 1971; Posey & Pierce, 1971). Waves from nuclear  
1200 explosions are also dispersive, such that in the far field the initial impulse becomes resolved into  
1201 a train of waves of decreasing period. Concerning volcanic eruptions, Bolt & Tanimoto (1981)

1202 and Mikumo & Bolt (1985) found atmospheric pressure waves from the 1980 Mount St. Helens  
1203 eruption with dominant periods of 5–8 min, while Kanamori et al. (1994) report atmospheric  
1204 oscillations with periods of 3–5 min for the 1883 Krakatoa, the 1982 El Chicón, and the 1991  
1205 Pinatubo eruptions as well.

1206 Acoustic waves with a period of ~5 min are thus often generated by energetic  
1207 atmospheric blasts. A recent analysis of HTHH air and seafloor pressure spectrograms by  
1208 Tonegawa & Fukao (2023) also identified long-continuing waves at frequencies near 3.6 mHz  
1209 (period of ~4.6 min), which bear a close resemblance to the trailing waves observed in our  
1210 satellite imagery. They argue that these waves represent the resonant coupling of the main Lamb  
1211 wave and thermospheric gravity waves that propagate horizontally at the sound speed. The long-  
1212 period primary Lamb wave can be adequately generated by a sea level or mid-tropospheric  
1213 pressure source (Amores et al., 2022; Watanabe et al., 2022). The excitation of the primary Lamb  
1214 wave together with the shorter period Lamb waves, thermospheric waves, and the resonant  
1215 waves, however, requires a more energetic pressure source located in the mesosphere.

1216 Besides the climactic explosion at ~04:29 UTC, Lamb waves were generated by the last  
1217 major explosion at ~08:40–08:45 UTC too. These weaker waves, however, could only be  
1218 observed in the near-field but not in the far-field domains. The mesoscale data also proved useful  
1219 to detect wind effects such as mean flow advection in the propagation of gravity waves and  
1220 captured gravity waves propagating near their theoretical maximum speed (~130 m s<sup>-1</sup> for a  
1221 wavelength of ~42 km).

1222 In conclusion, the GOES-R mesoscale observations represent a rich data source for  
1223 further work. More sophisticated analysis techniques (e.g., wavelet transform) could be used to  
1224 extract additional spectral information, confirm Lamb wave dispersion, and exploit IR channel  
1225 differences in order to characterize the 3D nature and vertical propagation of waves. The data  
1226 could also be used to constrain the HTHH eruption source parameters and validate the detailed  
1227 numerical modeling of global wave propagation.

1228

## 1229 **Acknowledgments**

1230 Á.H. was supported by the Deutsche Forschungsgemeinschaft (DFG) as part of the Research  
1231 Unit VollImpact, subproject VolPlume (FOR2820, DFG Grant 398006378). This study also  
1232 contributes to the Center for Earth System Research and Sustainability (CEN) of Universität  
1233 Hamburg. S.L.V. was supported by NSF Grant AGS-1832988. C.C.S. received funding from the  
1234 Minerva Fast Track Program of the Max Planck Society. The suggestions of Neil P. Hindley,  
1235 University of Bath, UK and two anonymous reviewers greatly improved the paper.

1236

1237 **Data Availability Statement**

1238 GOES-16 and GOES-17 datasets are publicly accessible through Amazon Web Services (AWS,  
1239 2023). ERA5 data are available from Hersbach et al. (2017). The Pago Pago, American Samoa  
1240 surface pressure data (sensor index 85435) are freely available for non-commercial use after  
1241 registration at PurpleAir (2023). The Coconut Point, American Samoa surface pressure data are  
1242 from the personal weather station of Joe LaPlante (joseph.laplante@noaa.gov) and are included  
1243 in the Supporting Information submitted with this paper. The publicly available ASOS Page 2  
1244 station data are provided by ASOS (2023).

1245 **References**

1246 Adam, D. (2022). Tonga volcano created puzzling atmospheric ripples. *Nature*, *602*, 497.

1247 <https://doi.org/10.1038/d41586-022-00127-1>

1248 Amores, A., Monserrat, S., Marcos, M., Argüeso, D., Villalonga, J., Jordà, G., & Gomis, D.

1249 (2022). Numerical simulation of atmospheric Lamb waves generated by the 2022 Hunga-Tonga  
1250 volcanic eruption. *Geophysical Research Letters*, *49*, e2022GL098240.

1251 <https://doi.org/10.1029/2022GL098240>

1252 ASOS. (2023). National Centers for Environmental Information (NCEI) [Dataset]. Retrieved

1253 from <https://www.ncei.noaa.gov/data/automated-surface-observing-system-one-minute-pg2/>

1254 Astafyeva, E., Maletckii, B., Mikesell, T. D., Munaibari, E., Ravanelli, M., Coisson, P., et al.

1255 (2022). The 15 January 2022 Hunga Tonga eruption history as inferred from ionospheric  
1256 observations. *Geophysical Research Letters*, *49*, e2022GL098827.

1257 <https://doi.org/10.1029/2022GL098827>

- 1258 Averiyarov, M., Ollivier, S., Khokhlova, V., & Blanc-Benon, P. (2011). Random focusing of  
1259 nonlinear acoustic *N*-waves in fully developed turbulence: Laboratory scale experiment. *Journal*  
1260 *of the Acoustical Society of America*, *130*(6), 3595–3607. <https://doi.org/10.1121/1.3652869>
- 1261 AWS. (2023). Amazon Web Services (AWS) [Dataset]. Retrieved from  
1262 <https://registry.opendata.aws/noaa-goes/>
- 1263 Bolt, B. A., & Tanimoto, T. (1981). Atmospheric oscillations after the May 18, 1980 eruption of  
1264 Mount St. Helens. *Eos Transactions American Geophysical Union*, *62*(23), 529–530.  
1265 <https://doi.org/10.1029/EO062i023p00529>
- 1266 Bór, J., Bozóki, T., Sători, G., Williams, E., Behnke, S. A., Rycroft, M. J., et al. (2023).  
1267 Responses of the AC/DC global electric circuit to volcanic electrical activity in the Hunga  
1268 Tonga-Hunga Ha'apai eruption on 15 January 2022. *Journal of Geophysical Research:*  
1269 *Atmospheres*, *128*, e2022JD038238. <https://doi.org/10.1029/2022JD038238>
- 1270 Bretherton, F. P. (1969). Lamb waves in a nearly isothermal atmosphere. *Quarterly Journal of*  
1271 *the Royal Meteorological Society*, *95*(406), 754–757. <https://doi.org/10.1002/qj.49709540608>
- 1272 Carr, J. L., Horváth, Á., Wu, D. L., & Friberg, M. D. (2022). Stereo plume height and motion  
1273 retrievals for the record-setting Hunga Tonga-Hunga Ha'apai eruption of 15 January 2022.  
1274 *Geophysical Research Letters*, *49*, e2022GL098131. <https://doi.org/10.1029/2022GL098131>
- 1275 Donn, W. L., & Ewing, M. (1962). Atmospheric waves from nuclear explosions—Part II: The  
1276 Soviet test of 30 October 1961. *Journal of the Atmospheric Sciences*, *19*(3), 264–273.  
1277 [https://doi.org/10.1175/1520-0469\(1962\)019<0264:AWFNEI>2.0.CO;2](https://doi.org/10.1175/1520-0469(1962)019<0264:AWFNEI>2.0.CO;2)

- 1278 Donn, W. L., Pfeffer, R. L., & Ewing, M. (1963). Propagation of air waves from nuclear  
1279 explosions. *Science*, *139*(3552), 307–317. <https://doi.org/10.1126/science.139.3552.307>
- 1280 Francis, S. H. (1973). Acoustic-gravity modes and large-scale traveling ionospheric disturbances  
1281 of a realistic, dissipative atmosphere. *Journal of Geophysical Research: Space Physics*, *78*(13),  
1282 2278–2301. <https://doi.org/10.1029/JA078i013p02278>
- 1283 Garrett, C. J. R. (1969). Atmospheric edge waves. *Quarterly Journal of the Royal*  
1284 *Meteorological Society*, *95*(406), 731–753. <https://doi.org/10.1002/qj.49709540607>
- 1285 GOES R. (2019). *GOES R Series Product Definition and User's Guide (PUG), 416-R-PUG-L1B-*  
1286 *0347 Vol. 3 Revision 2.2*. Retrieved from <https://www.goes-r.gov/users/docs/PUG-L1b-vol3.pdf>
- 1287 Harding, B. J., Wu, Y.-J. J., Alken, P., Yamazaki, Y., Triplett, C. C., Immel, T. J., et al. (2022).  
1288 Impacts of the January 2022 Tonga volcanic eruption on the ionospheric dynamo: ICON-  
1289 MIGHTI and Swarm observations of extreme neutral winds and currents. *Geophysical Research*  
1290 *Letters*, *49*(9), e2022GL098577. <https://doi.org/10.1029/2022GL098577>
- 1291 Heinrich, P., Gailler, A., Dupont, A., Rey, V., Hébert, H., & Listowski, C. (2023). Observations  
1292 and simulations of the meteotsunami generated by the Tonga eruption on 15 January 2022 in the  
1293 Mediterranean Sea. *Geophysical Journal International*, *234*(2), 903–914.  
1294 <https://doi.org/10.1093/gji/ggad092>
- 1295 Heki, K. (2022). Ionospheric signatures of repeated passages of atmospheric waves by the 2022  
1296 Jan. 15 Hunga Tonga-Hunga Ha'apai eruption detected by QZSS-TEC observations in Japan.  
1297 *Earth Planets Space*, *74*, 112. <https://doi.org/10.1186/s40623-022-01674-7>

- 1298 Hersbach, H., Bell, B., Berrisford, P., Hirahara, S., Horányi, A., Muñoz-Sabater, J., et al. (2017).  
1299 Complete ERA5 from 1940: Fifth generation of ECMWF atmospheric reanalyses of the global  
1300 climate [Dataset]. Copernicus Climate Change Service (C3S) Climate Data Store (CDS).  
1301 <https://doi.org/10.24381/cds.143582cf>
- 1302 Johnson, J. B., Boyer, T., Watson, L. M., & Anderson, J. F. (2023). Volcano opto-acoustics:  
1303 Mapping the infrasound wavefield at Yasur Volcano (Vanuatu). *Geophysical Research Letters*,  
1304 *50*, e2022GL102029. <https://doi.org/10.1029/2022GL102029>
- 1305 Kanamori, H., Mori, J., & Harkrider, D. G. (1994). Excitation of atmospheric oscillations by  
1306 volcanic eruptions. *Journal of Geophysical Research: Solid Earth*, *99*(B11), 21947–21961.  
1307 <https://doi.org/10.1029/94JB01475>
- 1308 Khaykin, S., Podglajen, A., Ploeger, F., Grooß, J.-U., Tence, F., Bekki, S., et al. (2022). Global  
1309 perturbation of stratospheric water and aerosol burden by Hunga eruption. *Communications*  
1310 *Earth & Environment*, *3*, 316. <https://doi.org/10.1038/s43247-022-00652-x>
- 1311 Kubota, T., Saito, T., & Nishida, K. (2022). Global fast-traveling tsunamis driven by  
1312 atmospheric Lamb waves on the 2022 Tonga eruption. *Science*, *377*(6601), 91–94.  
1313 <https://doi.org/10.1126/science.abo4364>
- 1314 Matoza, R. S., Fee, D., Assink, J. D., Iezzi, A. M., Green, D. N., Kim, K., et al. (2022).  
1315 Atmospheric waves and global seismoacoustic observations of the January 2022 Hunga eruption,  
1316 Tonga. *Science*, *377*(6601), 95–100. <https://doi.org/10.1126/science.abo7063>
- 1317 McCorkel, J., Van Naarden, J., Lindsey, D., Efremova, B., Coakley, M., Black, M., &  
1318 Krimchansky, A. (2019). GOES-17 Advanced Baseline Imager performance recovery summary.

- 1319 In *Proceedings of IGARSS 2019 – IEEE International Geoscience and Remote Sensing*  
1320 *Symposium*. Retrieved from <https://ntrs.nasa.gov/search.jsp?R=20190028689>
- 1321 Mikumo, T., & Bolt, B. A. (1985). Excitation mechanism of atmospheric pressure waves from  
1322 the 1980 Mount St Helens eruption. *Geophysical Journal International*, *81*(2), 445–461.  
1323 <https://doi.org/10.1111/j.1365-246X.1985.tb06412.x>
- 1324 Millán, L., Santee, M. L., Lambert, A., Livesey, N. J., Werner, F., Schwartz, M. J., et al. (2022).  
1325 The Hunga Tonga-Hunga Ha'apai hydration of the stratosphere. *Geophysical Research Letters*,  
1326 *49*, e2022GL099381. <https://doi.org/10.1029/2022GL099381>
- 1327 Nishida, K., Kobayashi, N., & Fukao, Y. (2014). Background Lamb waves in the Earth's  
1328 atmosphere. *Geophysical Journal International*, *196*(1), 312–316.  
1329 <https://doi.org/10.1093/gji/ggt413>
- 1330 Otsuka, S. (2022). Visualizing Lamb waves from a volcanic eruption using meteorological  
1331 satellite Himawari-8. *Geophysical Research Letters*, *49*, e2022GL098324.  
1332 <https://doi.org/10.1029/2022GL098324>
- 1333 Pierce, A. D., & Posey, J. W. (1971). Theory of the excitation and propagation of Lamb's  
1334 atmospheric edge mode from nuclear explosions. *Geophysical Journal International*, *26*(1-4),  
1335 341–368. <https://doi.org/10.1111/j.1365-246X.1971.tb03406.x>
- 1336 Posey, J. W., & Pierce, A. D. (1971). Estimation of nuclear explosion energies from  
1337 microbarograph records. *Nature*, *232*, 253. <https://doi.org/10.1038/232253a0>

- 1338 Proud, S. R., Prata, A. T., & Schmauss, S. (2022). The January 2022 eruption of Hunga Tonga-  
1339 Hunga Ha'apai volcano reached the mesosphere. *Science*, *378*(6619), 554–557.  
1340 <https://doi.org/10.1126/science.abo4076>
- 1341 Purkis, S. J., Ward, S. N., Fitzpatrick, N. M., Garvin, J. B., Slayback, D., Cronin, S. J., et al.  
1342 (2023). The 2022 Hunga-Tonga megatsunami: Near-field simulation of a once-in-a-century  
1343 event. *Science Advances*, *9*, eadf5493. <https://doi.org/10.1126/sciadv.adf5493>
- 1344 PurpleAir. (2023). PurpleAir, Inc. [Dataset]. Retrieved from <https://www2.purpleair.com/>
- 1345 Randel, W. J., Johnston, B. R., Braun, J. J., Sokolovskiy, S., Vömel, H., Podglajen, A., et al.  
1346 (2023). Stratospheric water vapor from the Hunga Tonga–Hunga Ha'apai volcanic eruption  
1347 deduced from COSMIC-2 radio occultation. *Remote Sensing*, *15*(8), 2167.  
1348 <https://doi.org/10.3390/rs15082167>
- 1349 Schmit, T. J., Griffith, P., Gunshor, M. M., Daniels, J. M., Goodman, S. J., & Lebar, W. J.  
1350 (2017). A closer look at the ABI on the GOES-R Series. *Bulletin of the American Meteorological*  
1351 *Society*, *98*(4), 681–698. <https://doi.org/10.1175/BAMS-D-15-00230.1>
- 1352 Sepúlveda, I., Carvajal, M., & Agnew, D. C. (2023). Global winds shape planetary-scale Lamb  
1353 waves. *Geophysical Research Letters*, *50*(19), e2023GL106097.  
1354 <https://doi.org/10.1029/2023GL106097>
- 1355 Stout, T. A. (2018). Simulation of N-wave and shaped supersonic signature turbulent variations,  
1356 (Doctoral dissertation). Retrieved from Electronic Theses and Dissertations for Graduate School  
1357 (ETDA). (<https://etda.libraries.psu.edu/catalog/15959tqs5346>). State College, PA: The  
1358 Pennsylvania State University.

- 1359 Suzuki, T., Nakano, M., Watanabe, S., Tatebe, H., & Takano, Y. (2023). Mechanism of a  
1360 meteorological tsunami reaching the Japanese coast caused by Lamb and Pekeris waves  
1361 generated by the 2022 Tonga eruption. *Ocean Modelling*, *181*, 102153.  
1362 <https://doi.org/10.1016/j.ocemod.2022.102153>
- 1363 Tonegawa, T., & Fukao, Y. (2023). Mesospheric pressure source from the 2022 Hunga, Tonga  
1364 eruption excites 3.6-mHz air-sea coupled waves. *Science Advances*, *9*(26), eadg8036.  
1365 <https://doi.org/10.1126/sciadv.adg8036>
- 1366 Vadas, S. L. (2013). Compressible  $f$ -plane solutions to body forces, heatings, and coolings, and  
1367 application to the primary and secondary gravity waves generated by a deep convective plume.  
1368 *Journal of Geophysical Research: Space Physics*, *118*(5), 2377–2397.  
1369 <https://doi.org/10.1002/jgra.50163>
- 1370 Vadas, S. L., Becker, E., Figueiredo, C., Bossert, K., Harding, B. J., & Gasque, L. C. (2023a).  
1371 Primary and secondary gravity waves and large-scale wind changes generated by the Tonga  
1372 volcanic eruption on 15 January 2022: Modeling and comparison with ICON-MIGHTI winds.  
1373 *Journal of Geophysical Research: Space Physics*, *128*, e2022JA031138.  
1374 <https://doi.org/10.1029/2022JA031138>
- 1375 Vadas, S. L., Figueiredo, C., Becker, E., Huba, J. D., Themens, D. R., Hindley, N. P., et al.  
1376 (2023b). Traveling ionospheric disturbances induced by the secondary gravity waves from the  
1377 Tonga eruption on 15 January 2022: Modeling with MESORAC/HIAMCM/SAMI3 and  
1378 comparison with GPS/TEC and ionosonde data. *Journal of Geophysical Research: Space*  
1379 *Physics*, *128*, e2023JA031408. <https://doi.org/10.1029/2023JA031408>

- 1380 Vadas, S. L., Yue, J., She, C.-Y., Stamus, P. A., & Liu, A. Z. (2009). A model study of the  
1381 effects of winds on concentric rings of gravity waves from a convective plume near Fort Collins  
1382 on 11 May 2004. *Journal of Geophysical Research: Atmospheres*, *114*, D06103.  
1383 <https://doi.org/10.1029/2008JD010753>
- 1384 Van Eaton, A. R., Lapierre, J., Behnke, S. A., Vagasky, C., Schultz, C. J., Pavolonis, M., et al.  
1385 (2023). Lightning rings and gravity waves: Insights into the giant eruption plume from Tonga's  
1386 Hunga Volcano on 15 January 2022. *Geophysical Research Letters*, *50*, e2022GL102341.  
1387 <https://doi.org/10.1029/2022GL102341>
- 1388 Vergoz, J., Hupe, P., Listowski, C., Le Pichon, A., Garcés, M. A., Marchetti, E., et al. (2022).  
1389 IMS observations of infrasound and acoustic-gravity waves produced by the January 2022  
1390 volcanic eruption of Hunga, Tonga: A global analysis. *Earth and Planetary Science Letters*, *591*,  
1391 117639. <https://doi.org/10.1016/j.epsl.2022.117639>
- 1392 Watada, S., Imanishi, Y., & Tanaka, K. (2023). Detection of air temperature and wind changes  
1393 synchronized with the Lamb wave from the 2022 Tonga volcanic eruption. *Geophysical*  
1394 *Research Letters*, *50*, e2022GL100884. <https://doi.org/10.1029/2022GL100884>
- 1395 Watanabe, S., Hamilton, K., Sakazaki, T., & Nakano, M. (2022). First detection of the Pekeris  
1396 internal global atmospheric resonance: evidence from the 2022 Tonga eruption and from global  
1397 reanalysis data. *Journal of the Atmospheric Sciences*, *79*(11), 3027–3043.  
1398 <https://doi.org/10.1175/JAS-D-22-0078.1>

- 1399 Winn, S., Sarmiento, A., Alferez, N., & Toubert, E. (2023). Two-way coupled long-wave  
1400 isentropic ocean-atmosphere dynamics. *Journal of Fluid Mechanics*, 959, A22.  
1401 <https://doi.org/10.1017/jfm.2023.131>
- 1402 Wright, C. J., Hindley, N. P., Alexander, M. J., Barlow, M., Hoffmann, L., Mitchell, C. N., et al.  
1403 (2022). Surface-to-space atmospheric waves from Hunga Tonga–Hunga Ha’apai eruption.  
1404 *Nature*, 609, 741–746. <https://doi.org/10.1038/s41586-022-05012-5>
- 1405 Yamada, M., Ho, T.-C., Mori, J., Nishikawa, Y., & Yamamoto, M.-Y. (2022). Tsunami triggered  
1406 by the Lamb wave from the 2022 Tonga volcanic eruption and transition in the offshore Japan  
1407 region. *Geophysical Research Letters*, 49, e2022GL098752.  
1408 <https://doi.org/10.1029/2022GL098752>
- 1409 Yuldashev, P. V., Ollivier, S., Karzova, M. M., Khokhlova, V. A., & Blanc-Benon, P. (2017).  
1410 Statistics of peak overpressure and shock steepness for linear and nonlinear *N*-wave propagation  
1411 in a kinematic turbulence. *Journal of the Acoustical Society of America*, 142(6), 3402–3415.  
1412 <https://doi.org/10.1121/1.5015991>